Wave enhancement due to a static electric field

S. I. Tsunoda and J. H. Malmberg
Department of Physics, University of California, San Diego, La Jolla, California 92093

(Received 3 March 1984; accepted 11 June 1984)

The effect of an applied static electric field on beam electrons trapped by the wave in a traveling wave tube has been investigated experimentally. For sufficiently weak applied fields the wave power is enhanced. When the applied field is sufficiently strong the beam electrons are detrapped, and the wave power enhancement is destroyed. It is found that the beam space charge plays an important role in the detrapping process and acts to limit the wave power enhancement. In addition it is found that the wave power enhancement can be increased by increasing the rf input drive level. By launching waves near the saturation level, over 10 dB of wave power enhancement has been observed. These effects are predicted in a computer simulation, and there is good agreement between the results of the simulation and the experimental results.

I. INTRODUCTION

It has been shown[1-4] theoretically that the application of a static force to particles trapped in the potential well of a wave can result in an increase in wave amplitude rather than a uniform acceleration of the particles. The basic mechanism of the effect can be understood by considering, in the rest frame of the wave, a single particle trapped in the potential well of the wave. Let us apply a weak, static force to the particle. Since the particle is trapped in the well of the wave, the response of the particle to the force cannot be a uniform acceleration because it is constrained to move at the essentially fixed phase velocity of the wave. Since the particle momentum cannot change in response to the applied force, the wave momentum changes. The wave momentum is proportional to the wave power, and hence, the wave power can be increased in this way. If instead we apply a force strong enough to detrap the particle, the particle accelerates, and the wave enhancement does not occur. This investigation is a study of this wave enhancement effect in a traveling wave tube[5] (TWT). We have observed the effect by applying a static electric field to beam electrons trapped in the potential well of a wave on the slow wave structure of a TWT. In the TWT the simple physical picture described above is complicated by the presence of many particles which are sloshing back and forth in the potential well. The particles not only feel the wave electric field and the static electric field, they also interact with one another through space-charge forces. This situation is further complicated by the oscillation of the potential well underneath the particles; that is, the wave phase velocity also oscillates.

In the TWT this effect was first studied theoretically by Hess.[1] Although the prospect of enhancing the power output beyond saturation was quite attractive, apparently his work was never followed up experimentally. There are, however, two related effects that have been studied both theoretically and experimentally. One effect involves the use of a voltage jump near the position of saturation along the tube. The idea is to sever the slow wave structure in such a way that the two pieces of the slow wave structure will support a large dc voltage jump while at the same time maintaining continuity for the propagating wave. As the wave is amplified, the beam slows down. At the position of wave power saturation, the beam velocity is a minimum. At this position the beam encounters the voltage jump. As it crosses the jump, the beam is reaccelerated so that it can again decelerate and give up more energy to the wave. This effect has been seen by Sauseng.[6] The other related effect is known as velocity tapering. By modifying the slow wave structure the wave phase velocity can be made to decrease as a function of axial distance. If the beam is still trapped, the beam momentum is thereby caused to decrease. The decrease in beam momentum causes an increase in wave momentum, and since the wave momentum is proportional to the wave power, the wave power increases. This effect was first studied theoretically by Meeker and Rowe.[7] In neither of these cases was the physics investigated very far beyond the region of saturation.

There are at least two other systems in which the wave enhancement effect can occur. It can occur[2] in a small cold beam plasma system,[8,9] where the beam is trapped in the potential well of a plasma wave. It can also occur[3,4] in a free electron laser[10] (FEL). In an FEL the beam is trapped in the beat wave due to an electromagnetic wave traveling in the presence of the spatially varying magnetic field of a wiggler. Although in this case the beam is relativistic, and the potential well is a magnetic well instead of an electrostatic well, there is a close relationship between the TWT and FEL, as has been pointed out by Kroll.[11]

In the small cold beam plasma system the effect was first studied theoretically by Morales.[2] His work was originally motivated by observations of runaway electrons in tokamaks. It was observed[12,13] that at low plasma densities the energy of the runaway electrons became clamped (that is, attained a constant value). At the same time electromagnetic radiation at the ion plasma frequency was observed. At higher plasma densities these effects were not observed. Morales' theory was developed in order to model these observations. This work was quickly followed by relativistic particle simulations by Leboeuf and Tajima[14] which supported the essential features of the theory.

In the FEL the application of a static electric field to trapped beam electrons has been proposed as a possible wave power enhancement scheme by Kroll *et al.*[3] and by Lin.[4] They have developed the theory of this enhancement scheme, but to date there has apparently been no experimental verification in FEL's.

In the present investigation we have verified the existence of this effect in a TWT. We have developed a technique

0031-9171/84/102557-19$01.90

for quantifying the wave enhancement that is observed, and we have found excellent agreement with theory. In the theory of the small cold beam plasma system, the space-charge electric field is always much smaller than the main wave electric field. However, in a TWT the space-charge electric field can be as large as the main wave electric field. We have found that the theory of the wave power enhancement is sensitive to the inclusion of space charge. We have also found that the extent of the wave power enhancement is sensitive to the rf input drive level. In particular, by launching waves at levels near the saturation level we have been able to increase the power to 10 dB above the saturation level.

The paper has been organized in the following manner. In Sec. II we review the linear and nonlinear theory of the TWT. In Sec. III we describe the experimental apparatus. In Sec. IV we present our results and in Sec. V our conclusions. In the Appendix we describe in detail the relationship between the TWT equations and the equations of the small cold beam plasma interaction.

II. THEORY

Here we review the one-dimensional theory of the TWT. The linear theory is taken from the theory of Pierce.[5] The basic procedure for the nonlinear theory presented here was given by Nordsieck.[15] This procedure was extended to include various corrections such as space charge and finite beam strength by Tien[16] and by Tien, Walker, and Wolontis.[17] Hess[1] further refined Tien's model and included the effect of the applied dc electric field. For reasons to be given below, Hess doubted the accuracy of his calculations when the space-charge correction was large. In Sec. II B we give a slightly different treatment of space charge which does not have these difficulties.

In both the linear and nonlinear theories the injected beam is assumed to be monoenergetic, and the spectrum is assumed to be a single wave. The interaction between the wave and the beam is governed by three equations—an inhomogeneous wave equation, Newton's law, and an equation of charge conservation. In the linear theory the beam is treated as a fluid, and harmonic solutions are assumed. The equations are solved in a Eulerian system, and an equation for the complex wavenumber is obtained. In the nonlinear theory, the dynamics of each beam electron are followed. The equations are cast in Lagrangian form, and the resulting equations are solved numerically.

A. Linear theory

In both the linear and nonlinear theories of the TWT presented here, the slow wave structure is represented by an equivalent one-dimensional transmission line. From the transmission line equations one can derive an inhomogeneous wave equation

$$\frac{\partial^2 V}{\partial z^2}-\frac{k_{0r}^2}{\omega^2}\frac{\partial^2 V}{\partial t^2}-2\frac{k_{0r}k_{0i}}{\omega}\frac{\partial V}{\partial t} = \frac{-Zk_{0r}}{\omega}\left(\frac{\partial^2\rho}{\partial t^2}+\frac{k_{0i}\omega}{k_{0r}}\frac{\partial\rho}{\partial t}\right), \qquad (1)$$

where V is the wave potential, ρ is the beam charge density (per unit length), ω is the angular frequency, and k_0 is the complex wavenumber in the absence of the beam; k_{0r} is its real part and k_{0i} is its imaginary part. Here Z is the interaction impedance of the line [whose real part is defined in Eq. (7)], z is the distance, and t is the time.

In addition, we have Newton's law that, in the absence of the static field, is

$$m\frac{du}{dt}=e\frac{\partial V}{\partial z}-eE_{\rm SC}\,, \qquad (2)$$

where u is the beam velocity, $E_{\rm SC}$ is the space-charge electric field, $-e$ is the electron charge, and m is the electron mass. We also have the equation of continuity,

$$\frac{\partial\rho}{\partial t}+\frac{\partial}{\partial z}(\rho u)=0\,. \qquad (3)$$

In the linear theory we let $\rho=\rho_0+\rho_1$ and $u=u_0+u_1$ and as usual assume ρ_0 and u_0 to be constant and ρ_1, u_1, and V to be harmonic perturbations of the form $e^{i(kz-\omega t)}$.

Pierce considers the perturbed charge density to capacitively couple to the slow wave structure through some effective capacitance per unit length C_1,

$$V_{\rm SC}=\rho_1/C_1\,, \qquad (4)$$

where $V_{\rm SC}$ is the space-charge potential. The above equations can be combined to form a determinantal equation for k

$$1=\frac{I_0k\omega/u_0}{2V_0(k-\omega/u_0)^2}\left(\frac{Zk_0k}{k_0^2-k^2}+\frac{k}{\omega C_1}\right), \qquad (5)$$

where $I_0=\rho_0u_0$ is the unperturbed beam current and $V_0=-mu_0^2/2e$ is the beam voltage. Because the slow wave structure is slightly lossy, k_0 and Z have small imaginary parts. The imaginary part of k_0 is kept in the resonant denominator and the imaginary part of Z is neglected.

In order to put this equation into scaled form, four parameters are defined by Pierce. The specification of these parameters completely characterizes the behavior in the linear regime for any given set of initial conditions.

The gain parameter C is defined by

$$C=(I_0R/4V_0)^{1/3}\,, \qquad (6)$$

where

$$R=\operatorname{Re}Z=\langle E_z^2\rangle_b/2k_{0r}^2P\,, \qquad (7)$$

where $\langle E_z^2\rangle_b$ is the square of the axial electric field averaged over the area of the beam. Here P is the total power of the wave. All quantities in Eq. (7) are defined in the absence of the beam. If we replace the slow wave structure interaction impedance R with the plasma impedance, then C is equivalent to $\eta'/2$, the smallness parameter of the spatial small cold beam theory.[9] This identity is discussed in detail in the Appendix. The detuning parameter b is

$$b=(u_0-v_0)/Cv_0\,, \qquad (8)$$

where $v_0=\omega/k_{0r}$, the phase velocity in the absence of the beam. The damping parameter d is defined by

$$d=k_{0i}/C(\omega/u_0)\,. \qquad (9)$$

The space-charge parameter is given by

$$QC=C/2u_0C_1R\,. \qquad (10)$$

Birdsall and Brewer[18] have shown the above expression to be equivalent to

$$QC = \frac{1}{4C^2}\left(\frac{\omega_q/\omega}{1+\omega_q/\omega}\right)^2, \tag{11}$$

where

$$\omega_q = P_q \omega_b\ , \tag{12}$$

where ω_b is the beam plasma frequency and P_q is the plasma frequency reduction factor[19] due to finite beam radius.

$$P_q = [1/(1+R_k^2)]^{1/2} \tag{13}$$

and

$$R_k = u_0\gamma/\omega r_b\ , \tag{14}$$

where r_b is the beam radius and γ is a geometrical factor of order unity and is a slowly varying function of $\omega r_b/u_0$.

If we now introduce the complex quantity δ by setting $k=(\omega/u_0)(1+iC\delta)$ and insert this expression along with the Pierce parameters into Eq. (5), we obtain

$$\begin{aligned}&\left(\delta+\frac{i\sqrt{4QC}}{1-C\sqrt{4QC}}\right)\left(\delta-\frac{i\sqrt{4QC}}{1+C\sqrt{4QC}}\right)\\ &\quad\times(\delta+ib+d)[C(\delta-ib-d)-2i]\\ &\quad=2(\delta C-i)^2\left(\frac{1+Cb-iCd}{1-4QC\,C^2}\right).\end{aligned}\tag{15}$$

Here C, b, d, and δ are measured quantities, and we use the above equation to determine QC.

B. Nonlinear theory

As in the linear theory, the charge distribution couples to the wave potential via Eq. (1). The wave potential together with the space-charge potential and the applied electrostatic potential affect the charge distribution through Newton's law

$$m\frac{d^2z}{dt^2} = e\frac{\partial V}{\partial z} - eE_{SC} - eE_{DC}\ , \tag{16}$$

where we have added E_{DC}, the applied static electric field. At any point z along the tube, the increment of charge about that point, $\rho(z,t)dz$, is equal to an amount of charge $\rho(z_0,0)dz_0$ at a point z_0 near the beginning of the tube where the density $\rho(z_0,0)$ is unmodulated.

$$\rho(z,t)dz = \rho(z_0,0)dz_0\ . \tag{17}$$

The three equations (1), (16), and (17) together with a method for calculating the space-charge potential provide a complete one-dimensional description of the TWT.

These equations are manipulated into a form suitable for calculation on a computer and are recast into scaled variables. The scaled distance along the tube is defined as

$$y = C(\omega/u_0)z\ . \tag{18}$$

And the input phase for an electron is

$$\phi_0 = (\omega/u_0)z_0\ . \tag{19}$$

We next define the dependent variables. The electron phase is defined as

$$\phi(y,\phi_0) = \omega(z/u_0 - t)\ . \tag{20}$$

The electron velocity, which defines $q(y,\phi_0)$, is

$$\frac{dz}{dt} = u_0[1+Cq(y,\phi_0)]\ , \tag{21}$$

and the wave potential, under the single wave assumption, is

$$V(z,t) = V_1(z,t) + V_2(z,t)\ , \tag{22}$$

where

$$V_1(z,t) = 4C^2V_0A(y)\cos[\phi-\theta(y)]\ , \tag{23}$$

$$\begin{aligned}V_2(z,t) &= [2C^3V_0/(1+Cb)]\\ &\quad\times\left[A\left(\frac{d\theta}{dy}+b\right)\cos(\phi-\theta) - \frac{dA}{dy}\sin(\phi-\theta)\right],\end{aligned}\tag{24}$$

where $A(y)$ is the scaled amplitude of the wave and $\theta(y)$ is the phase of the wave. Here $V_2(z,t)$ is a small correction to $V_1(z,t)$ due to the finite strength of the beam. It is discussed in detail in the Appendix. In scaled variables, Eqs. (1), (16), and (17) become

$$\frac{dA}{dy} = -Ad - \int_0^{2\pi}\frac{d\phi_0}{2\pi}\frac{\sin(\phi-\theta)}{1+Cq}, \tag{25}$$

$$\frac{d\theta}{dy} + b = \frac{1}{A}\int_0^{2\pi}\frac{d\phi_0}{2\pi}\frac{\cos(\phi-\theta)}{1+Cq}, \tag{26}$$

$$\frac{\partial\phi}{\partial y} = \frac{q}{1+Cq}, \tag{27}$$

$$\begin{aligned}(1+Cq)\frac{\partial q}{\partial y} &= 2A\sin(\phi-\theta) - C\left[\frac{dA}{dy}\cos(\phi-\theta)\right.\\ &\quad\left.+A\left(\frac{d\theta}{dy}-b\right)\sin(\phi-\theta)\right]\\ &\quad+(1/E_T)(E_{SC}+E_{DC}),\end{aligned}\tag{28}$$

where

$$E_T = 2(\omega/u_0)C^2V_0\ . \tag{29}$$

In these equations, terms of order C^2 and Cd have been neglected. The space-charge field is calculated in a manner similar to that described by Tien *et al.*[17] They represent the electrons as disks, and by using the Green's function for a disk inside a conducting cylinder of radius equal to the helix radius they find

$$\begin{aligned}E_{SC}/E_T &= 4\pi QC(1+R_k^2)\\ &\quad\times\int\frac{d\phi_0'}{2\pi}\exp[-R_k(1+Cq)|\phi(y,\phi_0')\\ &\quad-\phi(y,\phi_0)|]\operatorname{sgn}[\phi(y,\phi_0')-\phi(y,\phi_0)]\ .\end{aligned}\tag{30}$$

As Hess has pointed out, this method gives rise to a space-charge electric field that is a discontinuous function of distance. When two disks cross over each other, the space-charge force on a disk reverses direction discontinuously. These discontinuities produce errors that are of the same order as the value of the actual space-charge field. One way to overcome this is to treat the electrons as cylindrical blocks of charge. When two blocks cross over, the force on a block reverses sign smoothly. The blocks have a fixed width Δ. A slight modification to Eq. (30) thus gives

$$\frac{E_{SC}}{E_T} = 4\pi QC(1+R_k^2) \times \int \frac{d\phi_0'}{2\pi} \frac{\exp[-R_k(1+Cq)|\phi(y,\phi_0') - \phi(y,\phi_0) - \Delta/2|] - \exp[-R_k(1+Cq)|\phi(y,\phi_0') - \phi(y,\phi_0) + \Delta/2|]}{R_k \Delta}. \qquad (31)$$

In the actual computation where N particles are followed, Δ is equal to $2\pi/N$. This method of calculating the space-charge force is slightly different from the "compressible block" mode of Hess. As Hess points out, for large values of QC ($QC \gtrsim 0.28$) and large values of b ($b \gtrsim 1.5$), the compressible block method for calculating space charge results in a nonphysical behavior of the beam potential energy. He finds that at the start of the tube, the space-charge potential energy is zero since the beam is unmodulated there. However, in the nonlinear regime the space-charge potential energy becomes negative. This violates the requirement that the space-charge potential energy should be a minimum where the beam is unmodulated. In using Eq. (31), we find that the minimum always occurs at the beginning of the tube.

Since QC is typically 0.1–0.3 and R_k is typically 2–4, it can be seen from Eq. (31) that E_{SC} can be comparable to E_T. This behavior is in contrast to that in a small cold beam plasma system where E_{SC} is always small compared to E_T. The reason for the difference in E_{SC}/E_T between our TWT and the small cold beam plasma system is discussed in detail in the Appendix.

From Eqs. (25)–(28) we can derive conservation of momentum (neglecting terms of order C^2 and Cd)

$$\frac{d}{dy}\left(\frac{1}{1+Cb}\int_0^{2\pi}\frac{d\phi_0}{2\pi}q + A^2\right) = -2A^2 d + \frac{1}{1+Cb}\int_0^{2\pi}\frac{d\phi_0}{2\pi}\frac{E_{SC}+E_{DC}}{E_T}\frac{1}{1+Cq}, \qquad (32)$$

and conservation of energy (neglecting terms of order C)

$$\frac{d}{dy}\left[\int_0^{2\pi}\frac{d\phi_0}{2\pi}\frac{q^2}{2} + \left(2\frac{d\theta}{dy} + b\right)A^2\right] = -2\frac{d\theta}{dy}A^2 d + \int_0^{2\pi}\frac{d\phi_0}{2\pi}q\frac{E_{SC}+E_{DC}}{E_T}. \qquad (33)$$

When $b = d = QC = 0$, Eqs. (32) and (33) become (neglecting terms of order C)

$$\frac{d}{dy}\left(\frac{1}{2\pi}\int_0^{2\pi} q\, d\phi_0 + A^2\right) = \frac{E_{DC}}{E_T}, \qquad (34)$$

$$\frac{d}{dy}\left(\frac{1}{2\pi}\int_0^{2\pi}\frac{q^2}{2}d\phi_0 + 2\frac{d\theta}{dy}A^2\right) = \frac{1}{2\pi}\int_0^{2\pi} q\frac{E_{DC}}{E_T}d\phi_0. \qquad (35)$$

These are the spatial analogs of Morales'[2] Eqs. (34) and (35). From the conservation of momentum equation [Eq. (34)] we see that the static electric field is properly described as a force which causes an increase in either particle momentum or wave momentum or both. In general, both the particle and wave momentum increase. Since the wave power is proportional to the wave momentum, the wave power can be increased. If the beam were totally clamped (that is, if all the beam electrons have a constant velocity), the increase of the wave power would be secular, and the secular growth rate would be proportional to the strength of the applied field.

We have integrated Eqs. (25)–(28) numerically in the manner described by Hess. Just as in the experiment, the beam is assumed to enter the tube unmodulated. Thus, part of the initial wave amplitude is used to bunch the beam. Starting from this initially unmodulated state at the beginning of the tube, the phases and velocities of the beam particles as well as the wave amplitude and wave phase are calculated. The distance is then stepped forward and the calculations are repeated. The step size is $\Delta y = 0.01$ and we use $N = 100$ beam electrons. As a check on the accuracy of this procedure we compute and compare the left-hand side and right-hand side of Eq. (32). A and q are of order unity in the nonlinear region and the discrepancy is always less than 0.02.

III. EXPERIMENTAL APPARATUS AND LINEAR PROPERTIES

In this section we describe the characteristics of our TWT, the means by which the static electric field is produced, and the experimental technique. In order to compare theory with experiments in the nonlinear regime, we experimentally determine the Pierce parameters in the linear regime of the tube. The methods by which these parameters are measured are described in Sec. III B.

A. Experimental apparatus

The TWT used in this experiment, which has been described in detail elsewhere,[20] is much longer in scaled units than commercially available TWT's. Commercially available TWT's are generally 5–8 e-folding lengths long. Because we are interested in the interaction region beyond saturation, our TWT was designed to be approximately 20 e-folding lengths long. Our TWT also has axially moveable rf probes which allow us to measure the wave power as a function of axial distance. Commerically available TWT's generally have their output coupler fixed at the position of saturation.

The apparatus is shown schematically in Fig. 1. The beam is formed by a Pierce type electron gun. The source filament is a directly heated flat spiral of 2% thoriated tungsten wire. The wire diameter is 0.043 cm. The spiral has 3½ turns and is 0.89 cm in diameter. The filament and the forming electrodes are biased negatively. We can independently vary the beam voltage between 40–150 V and the beam current between 0–1.2 mA. The beam radius is 0.39 cm. The

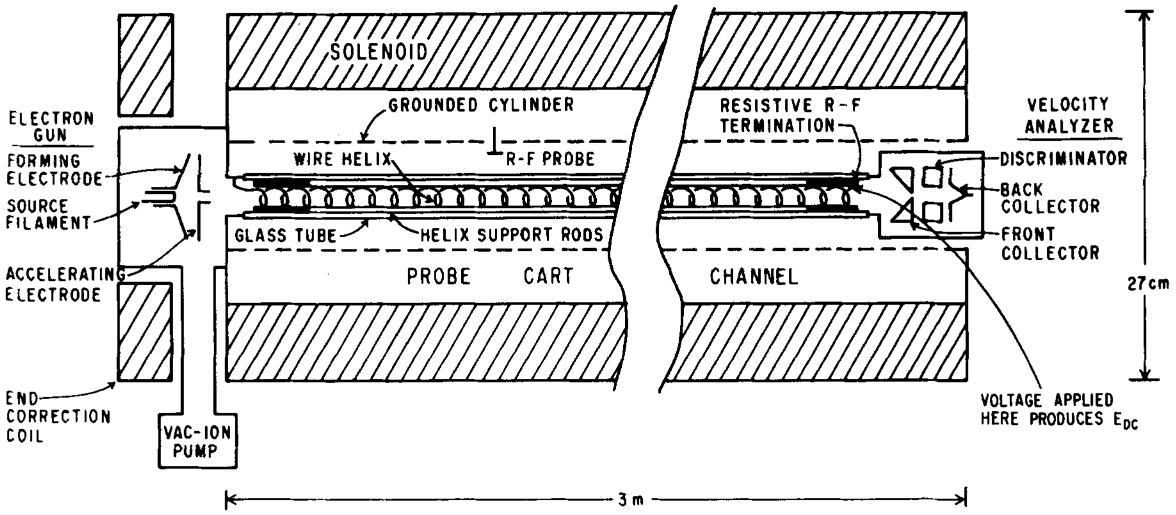

FIG. 1. Schematic diagram of the apparatus (not drawn to scale).

electrons are directed along the axis of the helix and are radially confined by a strong axial magnetic field whose on axis value is $B_z = 385$ G. In addition there are two magnetic field coils (not shown) which provide perpendicular magnetic fields (B_x and B_y). These coils are used to control the tilt of the beam with respect to the helix axis. The electron beam is pulsed by applying a square pulse to the accelerating electrode. This is done in order to keep the ion density in the system low. The electron beam produces ions due to collisions of the beam electrons with the residual gas background. The ions leave the beam region by following the magnetic field lines to the gun and collector. If the production rate is greater than the loss rate, the ions accumulate, and the resulting ion noise can produce undesirable effects. Pulsing the beam keeps the ion production rate low and keeps the tube substantially free of ions. The time duration of the current pulse is 180 μsec. The pulse repetition rate is 60 Hz. The transit time of the beam is approximately 0.5 μsec. After passing through the helix, most of the beam is collected by the front collector of the velocity analyzer. A small fraction (approximately 0.5%) of the beam passes through a hole in the front collector and through the discriminator ring and is collected by the back collector. By biasing the discriminator ring and measuring the current collected at the back collector, we can determine[21] the velocity distribution function of that portion of the beam which passed through the front collector. The region containing the electron gun, helix, and velocity analyzer is evacuated. The pump pressure is typically 3×10^{-8} Torr. We estimate the pressure at the midpoint of the tube to be about 1×10^{-6} Torr.

The heart of the TWT is the helical slow wave structure. The helix is 2.7 m long and composed of 0.051 cm diam Be–Cu wire which is held rigid by four alumina rods glued to the outside of the wire helix. The pitch of the helix is 0.079 cm and its outside diameter is 2.21 cm. At each end of the helix is a resistive rf termination which serves to reduce reflections. The termination consists of carbon-impregnated paper which is glued onto the windings of the helix. Each termination is 13.7 cm long, and one end of the carbon-impregnated paper is flush with the end of the helix. Reflected waves originate from slight irregularities in the radius and pitch of the helix as well as from the ends. The maximum VSWR is 1.26. Because the backward wave is far from synchronism with the beam, the effect of the backward wave on the beam dynamics is negligible. The helix assembly is enclosed by a glass vacuum jacket which is in turn enclosed by an axially slotted 3.8 cm radius cylinder which defines the rf ground. Inside the cylinder but outside the vacuum jacket are four axially moveable rf probes. The probes couple capacitively to the helix. The frequency range of the launched waves is typically 5–100 MHz. The cylinder, which has a cutoff frequency of 3.0 GHz, is a waveguide beyond cutoff for the frequencies used in the experiment. This ensures (assuming the receiving probe is more than 5 cm away from the transmitting probe) that the received waves are helix traveling modes and prevents any direct coupling between the transmitting and receiving probes.

The static electric field is created by applying a potential to the end of the helix near the collector. The end of the helix near the gun is grounded. Thus the electric field extends along the entire length of the helix. The potential is not continuously held constant because for potential above 100 V, too much power is absorbed by the helix due to ohmic heating, and the helix support structure begins to deteriorate. In order to avoid this, the potential is pulsed. The duration of the pulse is 31 μsec. Since this is much longer than the beam transmit time (typically 0.5 μsec), the electrons see an essentially uniform, static electric field. The pulsed potential can be varied from 0 to 1.5 kV.

The timing sequence is as follows. Initially the accelerating electrode is held at a more negative potential than the cathode. To initiate the beam current pulse the accelerating electrode potential is brought abruptly to ground. Eighty microseconds later the helix potential is pulsed and 10 μsec later the data are taken. Finally, 70 μsec after the data are taken the beam current pulse terminates as the accelerating electrode potential is brought back below the cathode potential. This sequence is repeated 60 times a second. The filament heating power and the transmitter are on continuously.

The receiver consists of a calibrated probe followed by a step attenuator and a low noise amplifier. The amplifier output is split into two parts. One part is fed into a high-frequency (> 60 MHz) scope in order to monitor the waveform. The other part is put through a low pass filter, which rejects the harmonics, and is then detected. The detected output is amplified and sampled and held. The sample and hold is gated 10 μsec after the helix potential is pulsed. The held output is put through a logarithmic amplifier and into the Y channel of an X–Y recorder. A voltage proportional to the axial position of the probe is put into the X channel of the X–Y recorder. The probe is moved along the helix and thereby plots of the wave power versus axial distance are produced. The probe coupling is calibrated using the three-probe coupling technique.[21] The probe coupling is determined to an accuracy of 3 dB.

B. Linear properties

Figure 2 shows a plot of the measured and theoretical helix dispersion. The measured dispersion is determined with a standard interferometer technique.[22] The theoretical dispersion is calculated assuming the Pierce sheath helix model[5] and assuming that the dielectric constant of the shell-like region between the helix and the glass vacuum jacket is a constant whose value is the area weighted average of the rod and vacuum dielectric constants.

$$\epsilon_{\text{effective}} = (4A_r/A_s)(\epsilon_r - 1) + 1 , \qquad (36)$$

where $\epsilon_r = 8.6$ is the dielectric constant of the four alumina rods and A_r and A_s are the cross-sectional areas of a rod and the shell, respectively. The measurements are within 0.8% of the corresponding theoretical values. There are no adjustable parameters.

The imaginary part of the wavenumber in the absence of the beam, k_{0i}, is determined by directly measuring the power as a function of axial distance. The loss tangent, k_{0i}/k_{0r}, is 2.2×10^{-3} at 20 MHz and rises slowly to 4.2×10^{-3} at 90 MHz. At 40 MHz, the total attenuation over the entire length of the tube is 4.0 dB; at 60 MHz, it is 9.2 dB.

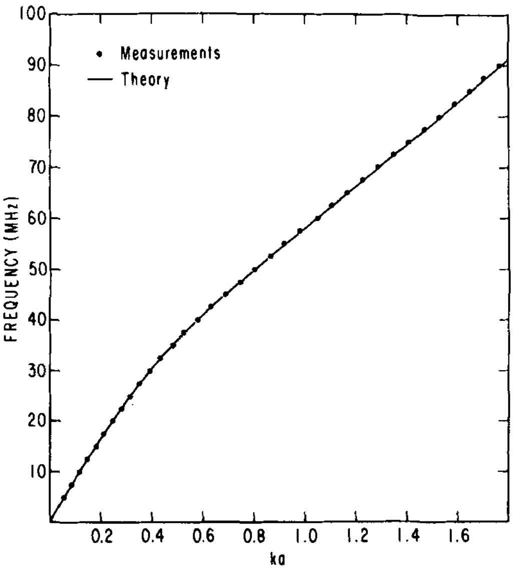

FIG. 2. Dispersion relation for the slow wave structure. The points are the measured results, and the line is the result of calculation. $a = 1.08$ cm is the helix radius.

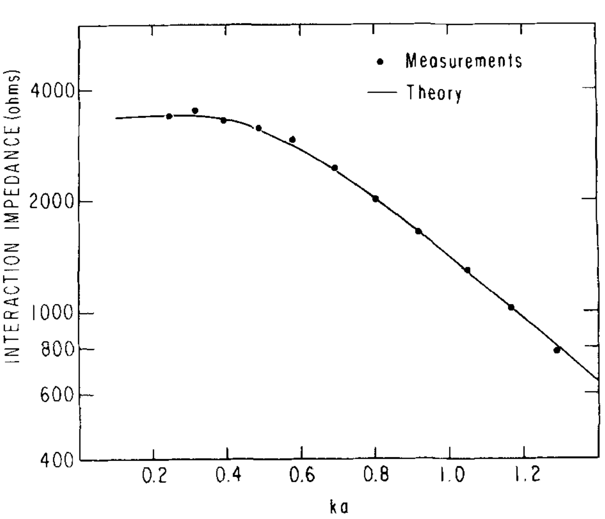

FIG. 3. Interaction impedance of the slow wave structure. The points are the measured results, and the line is the result of calculation.

There are five parameters which completely characterize the interaction in one-dimensional TWT theory. They are the gain parameter C, the damping parameter d, the detuning parameter b, and the two space-charge parameters QC and R_k. We now describe the methods we use to experimentally determine these parameters. Many of these methods are described in detail elsewhere.[20]

In order to determine the gain parameter we must first determine the interaction impedance R. The interaction impedance is theoretically calculated using Eq. (7). It is experimentally determined using the Kompfner dip technique.[23,24] Figure 3 shows a plot of the measured and theoretical impedance. The measurements are within 4% of the corresponding theoretical values. Here C is then computed using Eq. (6).

The damping parameter is determined from Eq. (9), with k_{0i} directly measured as previously described.

The detuning parameter is a measure of the difference between the beam velocity and the wave phase velocity in the absence of the beam. The wave phase velocity is accurately known because we measure the frequency and wavenumber independently in order to determine the dispersion relation. TWT theory assumes that the beam is monoenergetic. For most of the experimental data the beam has a 1–2 V shear which is due to the Ohmic drop across the filament. We have checked that this shear is unimportant by pulsing the potential across the filament and comparing wave power plots taken with and without the Ohmic drop across the filament. The beam velocity is measured in several ways. First, by measuring the dispersion relation of a sufficiently weak beam of high enough velocity so that there is no beam helix interaction, one can infer the beam velocity. The experimental error in this procedure is less than 2%. Second, again for noninteracting electron beams, the beam energy can be directly measured using the velocity analyzer. The values obtained using this method agree with those obtained using the first within 1%. Third, for interacting beams, the detuning parameter b can be measured using the Kompfner dip technique. The accuracy obtained with this technique is $\Delta b = \pm 0.12$. This corresponds to an experimental error in velocity of 1.0%. All three methods agree with each other within experimental error.

The space-charge parameters are given by Eqs. (11)–(14). In order to determine them one of the quantities that must be measured is the beam radius. The beam radius is measured by varying the perpendicular magnetic fields (B_x and B_y) which tilt the beam and measuring the current that passes through the hole in the center of the front collector as a function of beam tilt. By measuring the beam current and voltage, ω_b can be determined. Thus, in order to determine QC and R_k, all that remains is to determine γ. Here γ is a geometrical parameter, and it is a slowly varying function of $\omega r_b/u_0$. We determine it as follows. We first determine the functional dependence of γ on $\omega r_b/u_0$ for noninteracting beams, that is, beams that are of high enough velocity that they do not excite growing modes. The dispersion relation for such a beam is

$$\omega = k_F u_0 + \omega_q \,, \quad \omega = k_S u_0 - \omega_q \,, \tag{37}$$

where k_F corresponds to the fast wave and k_S corresponds to the slow wave. We measure ω, k_S, and k_F and thereby determine γ through Eqs. (12)–(14) and (37). Figure 4 shows a plot of γ vs $\omega r_b/u_0$ for five different noninteracting beams. The best fit straight line through these points yields

$$\gamma = 1.06[(\omega/u_0)r_b] + 0.682 \,. \tag{38}$$

We use this form for γ to calculate QC which in turn is used in Eq. (15) to calculate linear growth rates. Figure 5 shows the comparison between the measured growth rates and the theoretical growth rates which have been calculated in this way. The growth rates are plotted versus b and have been normalized to $C\omega/u_0$. The dots are the measured values and the lines are the calculated values for γ, $\gamma + 0.1$, and $\gamma - 0.1$. It is seen that the linear growth measurements agree with the wave dispersion measurements to $\gamma \pm 0.1$.

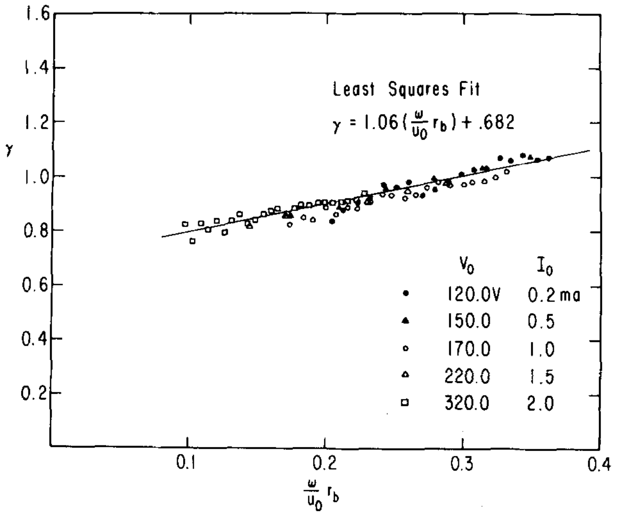

FIG. 4. The geometrical parameter γ vs $\omega r_b/u_0$ for five different beams.

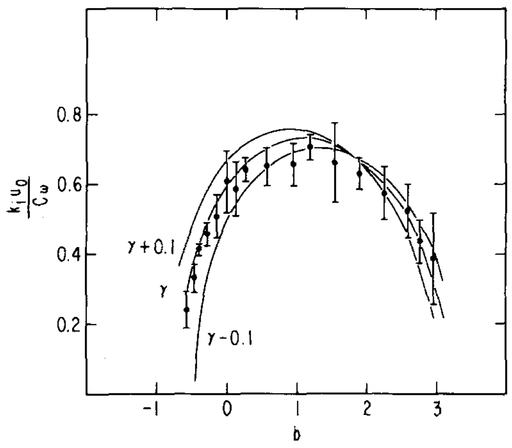

FIG. 5. Normalized linear growth rate $k_i u_0/C\omega$ vs detuning parameter b. Lines are calculated for γ, $\gamma \pm 0.1$. Points are the measured results.

IV. RESULTS

We present our basic findings in this section. We first demonstrate the existence of the effect and give a method for quantifying the degree of wave power enhancement. Using this method we show that there is good quantitative agreement between the experiment and the computer simulation. The effect is seen to be sensitive to the inclusion of space charge in the theory, to the position along the tube where the field is first applied, and to the strength of the rf input drive level. The phase space plots generated in the simulation are used to understand the process of detrapping.

A. Existence of the effect

In Fig. 6, we exhibit an example of wave power versus axial distance from the transmitter. Consider first the solid curve. The wave power is seen to grow linearly up to about $z = 40$ cm. Wave power saturation occurs around $z = 55$ cm, and the wave power then undergoes the familiar trapping oscillations. By the level of saturation, we mean the level of the first relative maximum. Three trapping oscillations are clearly seen. The slight damping evidenced here is due to the dissipation in the helix support structure. The fast

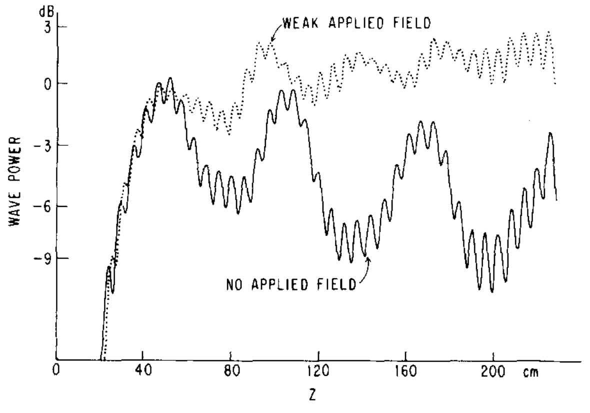

FIG. 6. Wave power versus axial distance with and without a weak static field applied. Solid curve: $E_{DC} = 0$, $V_0 = 97.4$ V, $I_0 = 1.1$ mA, $\omega/2\pi = 40.0$ MHz. Dotted curve: $E_{DC} = 0.535$ V/cm, $V_0 = 85.8$ V. All other parameters are the same as for the solid curve. 0 dB corresponds to 30.9 mW.

oscillations are a beat between the forward wave and a small component of backward wave. Since the backward wave is far out of synchronism with the beam, its interaction with the beam is negligible.

When we apply a weak static electric field (which is applied along the entire length of the helix), the result is the dotted curve in Fig. 6. The sense of the field is such that in the absence of the wave the field would increase the velocity of the beam. The beam voltage has been changed so that at the position of saturation ($z = 55$ cm), the power levels are the same. This is done in order to emphasize the enhanced growth beyond saturation. We see that not only has the wave power overcome the damping due to the dissipation in the helix support structure, but it has also grown by about 3 dB above the saturation level. The trapping oscillations indicate the presence of trapped particles, and we see that the application of a force to these trapped particles has resulted in an increase in wave momentum and hence in wave power. When we apply a strong static electric field, we obtain the dotted curve in Fig. 7. Again the solid curve is the zero field case. And again the beam voltage has been changed to make the power levels at $z = 55$ cm the same. Although power level of the first relative maximum ($z = 60$ cm) is higher than the level at $z = 55$ cm, we see that beyond $z = 60$ cm, the wave enhancement is destroyed in the presence of a strong applied field. The absence of wave enhancement is to be expected for fields so strong that particle detrapping occurs, and the result of the applied force is then an increase in beam momentum rather than wave momentum. The reason the power level at $z = 60$ cm is so high is that most of the electrons remain trapped up to this point. Even for large static fields some electrons that later become runaways remain trapped prior to saturation and contribute to the wave growth prior to saturation. So that prior to the saturation regime of the tube, the wave power can be enhanced. In Fig. 8 we show the result of applying a static electric field in the reversed sense; that is, the sense in which in the absence of the wave, the static field would decrease the beam velocity. As expected, the response to the force is a decrease in wave momentum and hence in wave power, and so the result is enhanced damping.

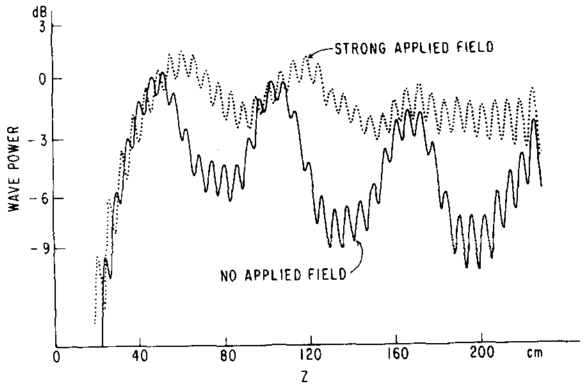

FIG. 7. Wave power versus axial distance with and without a strong static field applied. Solid curve: same as parameters for solid curve in Fig. 6. Dotted curve: $E_{DC} = 0.665$ V/cm, $V_0 = 112$ V. All other parameters are the same as for the solid curve.

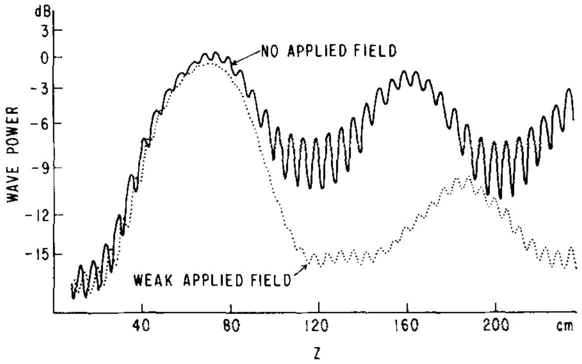

FIG. 8. Wave power versus axial distance with the static field applied in the reversed sense (dotted curve). $E_{DC} = -0.147$ V/cm, $V_0 = 81.0$ V, $I_0 = 0.2$ mA, and $\omega/2\pi = 40.0$ MHz. For comparison, a case with no static field applied is shown (solid curve). In this case, $V_0 = 76.4$ V, $I_0 = 0.2$ mA, and $\omega/2\pi = 40.0$ MHz. 0 dB corresponds to 8.11 mW.

B. Fourier analysis of wave power plots

In order to quantify the degree of wave power enhancement, we would like to assign a slope to the wave power plot in the region beyond saturation. Here a difficulty arises due to the presence of the trapping oscillations. Typically, the average rate of power enhancement is much smaller than the large growth and damping rates associated with the trapping oscillations. In addition, the power variation is affected by the dissipative damping due to the helix. Thus, the determination of the proper slope is not easily made from a casual inspection of the data. However, a method for determining the proper slope is suggested by the following considerations. Equation (34) expresses conservation of momentum for $b = d = QC = 0$ and $C \ll 1$. The first term on the left-hand side corresponds to the beam momentum, and the second term corresponds to the wave momentum. Let us assume all the electrons are trapped. If we average over the trapping oscillations, the first term vanishes and we obtain

$$\frac{d}{dy}\langle A^2\rangle = \frac{E_{DC}}{E_T}. \tag{39}$$

So in this ideal case, the slope of the wave momentum or wave power averaged over the trapping oscillations is a constant, and the constant is proportional to the strength of the applied static field. Figure 9(a) shows an example of raw data. The first step in the data analysis is to consider only that portion of the power plot past saturation and to remove the fast oscillations in the plot by drawing a smooth curve through the fast oscillations. The curve passes through the geometric mean of the maxima and minima of the fast oscillations. Since the fast oscillations have peak-to-peak amplitudes typically between 1–3 dB, the error incurred in using the geometric mean to describe the forward traveling wave is 0.17%–1.5%. The data are then put on a linear scale. Now, again from conservation of momentum, this time including damping, we have

$$\frac{d}{dy}\left(\int_0^{2\pi}\frac{d\phi_0}{2\pi}q + A^2\right) = -2A^2 d + \frac{E_{DC}}{E_T}. \tag{40}$$

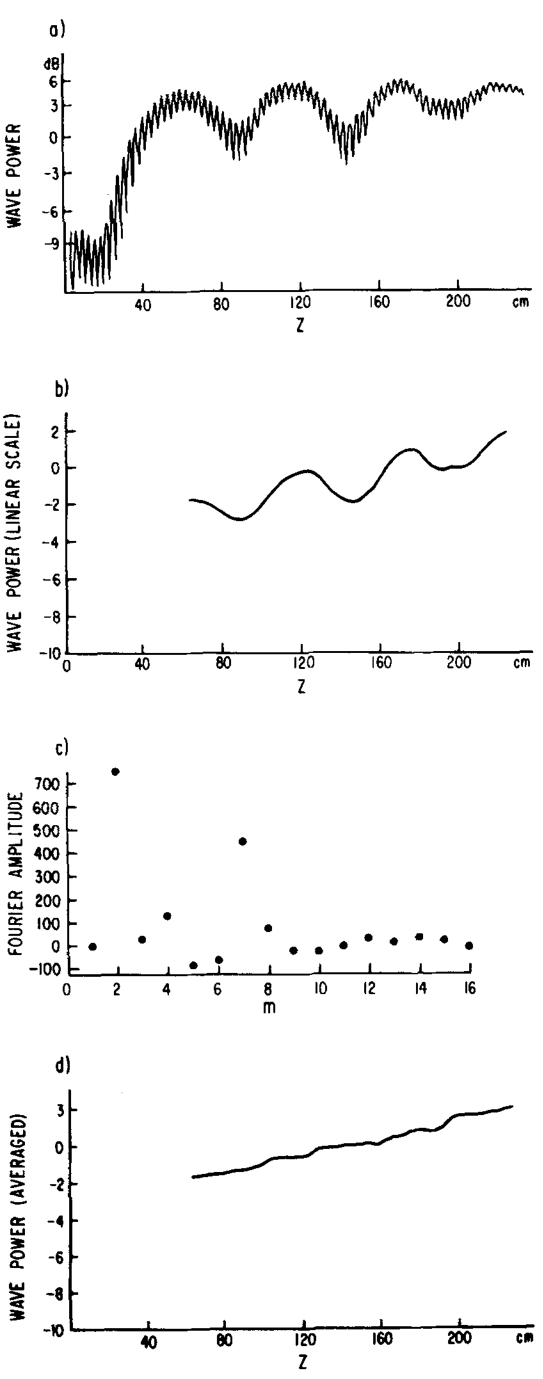

FIG. 9. An example illustrating the data analysis procedure. (a) Typical example of raw data. The experimental parameters are the same as those in Fig. 10. $E_{DC}/E_T = 0.307$. (b) The portion of the raw data beyond saturation has been put on a linear scale and corrected for damping and filtered. (c) The corrected plot is Fourier transformed. The real part is shown here. (d) Inverse Fourier transform of (c) after the trapping oscillations have been filtered out.

If

$$A^{2\prime} = A^2 + \int_{y_{\text{sat}}}^{y} 2\,dA^2(y)dy, \tag{41}$$

then

$$\frac{d}{dy}\left(\int_0^{2\pi}\frac{d\phi_0}{2\pi}q + A^{2\prime}\right) = \frac{E_{DC}}{E_T}, \tag{42}$$

and in the case of 100% trapping, we would have

$$\frac{d}{dy}\langle A^{2\prime}\rangle = \frac{E_{DC}}{E_T}, \tag{43}$$

where we average over the trapping oscillations as in Eq. (39). So we use Eq. (41) to correct for the effect of the damping due to helix structure dissipation. The Pierce parameter d in Eq. (41) is a measured quantity. At this point the power plot takes the form of Fig. 9(b). Next, the length of the abscissa is doubled by reflecting the data about a vertical line at the left edge of the curve ($z = 60$ cm) in Fig. 9(b). The doubled curve resembles one period of a sawtooth wave with a sine wave superimposed on it. The data are then Fourier transformed. The real part of the transformation is shown in Fig. 9(c). The peaks in the Fourier transform at $m = 7,8$ corresponds to the trapping oscillations. The next step in the procedure is to get rid of the trapping oscillations by applying a square bandstop filter to both the real and the imaginary parts of the spectrum. The center of the filter is positioned at the mode number of the largest peak away from the peaks at $m = 1 - 4$. The full width of the filter is equal to the mode number at the center of the filter minus two. So in this example the bandstop filter would extend from $m = 5$ to $m = 9$. The real part of the inverse Fourier transform is shown in Fig. 9(d). The result is very nearly a straight line. Finally, the slope of this straight line is calculated with a least squares fit. To see how sensitive this procedure is to the nature of the filter, we have tried a variety of different widths of square bandstop filters and Gaussian filters. The resulting slopes were found to be essentially insensitive to the type of filter used. We also calculate the imaginary part of the inverse Fourier transform. Its smallness (typically $< 10^{-4}$) is a measure of the integrity of the transform procedure.

The procedure is applied to the experimental power plots and the simulation power plots in exactly the same way. In particular, damping is included as an input parameter of the simulation. The computer generated power plot is then corrected for damping in the manner described above.

C. Dependence of secular growth rate on applied field strength

Having developed a procedure for determining the slope of the enhanced wave power growth; that is, the secular growth rate, we can plot these growth rates versus the applied static electric field strengths. This is done in Fig. 10. The ordinate and abscissa are labeled in scaled dimensionless units. The secular growth rate scaling involves $z_L = u_0/C\omega$ and $P_s = 2CI_0V_0$ which correspond physically to the linear e-fold distance and the saturation power, respectively. The applied static electric field is scaled to $E_T = 2C^2V_0\omega/u_0$, the main wave field strength near saturation. When these scalings are used, Eq. (43), which describes the ideal case of $QC = 0$ and $C \ll 1$ and 100% trapping, would be plotted as a 45° line in Fig. 10 (and in Figs. 14 and 16). The solid dots are the results of the experiment. As we would expect, the secular growth rate at first increases as the static electric field strength increases and then decreases as beam particles detrap and run away. In the data set of Figs. 6, 7, and 8 the beam voltage is changed in order to emphasize the behavior of the wave power in the nonlinear regime. In the data set of

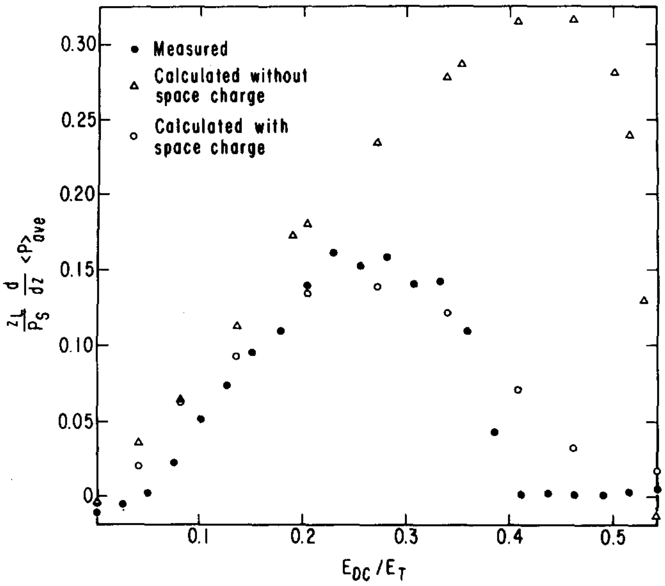

FIG. 10. Normalized secular growth rate versus normalized static field strength E_{DC}/E_T. $V_0 = 42.6$ V, $I_0 = 0.10$ mA, and $\omega/2\pi = 60.0$ MHz. $z_L = 11.3$ cm, $P_s = 0.995$ mW, and $E_T = 0.685$ V/cm. $C = 0.0909$, $b = 0$, $d = 0.0498$, $QC = 0.181$, and $R_k = 3.10$. The solid points are the measured results. The open circles are the computed results including the space charge force. The open triangles are the computed results neglecting the space charge force.

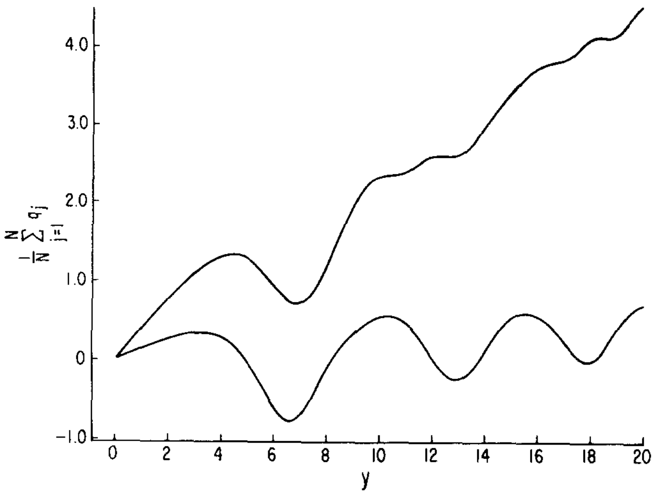

FIG. 11. Computed normalized average particle momentum versus scaled distance. The bottom curve corresponds to the open circle at $E_{DC}/E_T = 0.136$ in Fig. 10. The top curve corresponds to the open circle at $E_{DC}/E_T = 0.407$ in Fig. 10.

Fig. 10 the beam voltage is kept at a constant value so that all the data correspond to the same values of the Pierce parameters. As was mentioned in Sec. III, there is a resistive rf termination placed at each end of the helix. In order to effectively launch waves, the transmitter probe must not be directly over the rf termination; it must be placed at some distance away from the edge of the helix. In this case the distance between the end of the helix and the transmitter is 16.6 cm. In order to keep the injected beam voltage constant as the applied field strength is increased, it is necessary to increase the cathode voltage (that is, make it less negative) because the portion of the helix between the gun end of the helix and the transmitter accelerates the beam electrons before they reach the z coordinate of the transmitter. Thus, at each value of the applied field strength the cathode voltage was increased by 6.19% of the applied helix voltage in order to compensate for this additional acceleration. The open circles are the results of the computer simulation for the corresponding Pierce parameters of the experiment. The input parameters in the simulation are the same as those in the experiment. In order to obtain the best fit to the experiment, some of the input parameters have been adjusted slightly. However, each input parameter is within the experimental error of the corresponding experimental value. No other adjustments have been made.

In Fig. 11 we plot the computed normalized average particle momentum as a function of scaled distance for the open points at $E_{DC}/E_T = 0.136$ and $E_{DC}/E_T = 0.407$. The input particle momentum has been subtracted from the particle momentum and the result has been averaged over the particles and divided by C. The distance is scaled by $\omega C/u_0$. The plot corresponding to $E_{DC}/E_T = 0.136$ (bottom curve) shows the normalized average particle momentum increasing due to the applied electric field until $y = 3.5$, where it begins to decrease. There is a minimum in the average particle momentum at $y = 6.6$. Beyond $y = 6.6$ the average particle momentum oscillates as the trapped particles execute their orbits in phase space. When the applied field strength is increased to $E_{DC}/E_T = 0.407$ (top curve), the normalized average particle momentum continues to increase beyond $y = 7.0$ as particles become detrapped and run away.

D. Effect of space charge

Space charge can play a very important role in the enhancement process. The computer results (open circles) of Fig. 10 include the space-charge force. If we do not include the space-charge force, the result is the set of triangular points in Fig. 10. It is seen that the inclusion of space charge in the calculation significantly limits the extent of the wave power enhancement.

The space-charge force plays an important role in the wave power enhancement because it can be as strong as the wave field itself. Figure 12 is a plot of the space-charge electric field felt by a single representative electron as a function of distance down the tube. The abscissa is scaled to the linear e-folding distance, and the ordinate is scaled to the main wave field strength E_T. The main wave amplitude at saturation is approximately $2E_T$. Thus, it is seen that the space-charge electric field strength is comparable to the saturation field strength at certain points along the tube.

The particle dynamics in this system are complicated for the following reasons: the wave amplitude is a function of distance along the tube; the potential well oscillates underneath the particles; and the magnitudes and directions of the space charge forces vary rapidly as the particles execute their motions. The description is further complicated by the fact that the linear wave growth, the wave phase oscillations, and the trapping oscillations all have the same length scale. We have not been able to invent any model that both simplifies the particle dynamics and describes all of the essential phys-

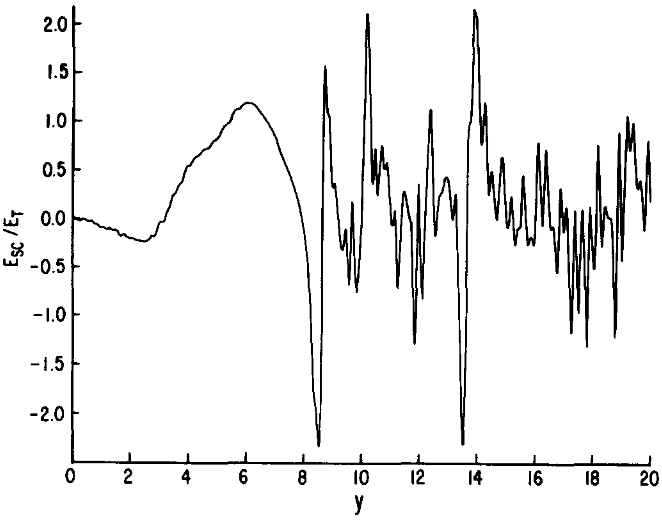

FIG. 12. Computed normalized space-charge electric field felt by a typical particle versus scaled distance. The Pierce parameters correspond to those of Fig. 10. $E_{DC}/E_T = 0.339$.

ics. The best way to understand the particle dynamics is to study in detail their phase space trajectories.

The phase space trajectories of the particles with and without space charge included in the simulations are fundamentally different. This is demonstrated in Fig. 13. On the left from top to bottom are phase space plots which have been calculated without space charge. The ordinate is the scaled particle velocity q defined by $dz/dt = u_0(1 + Cq)$. The abscissa is the particle phase minus the wave phase, $\phi - \theta$. The plots shown from top to bottom are selected phase space plots at certain positions along the tube away from the transmitter. On the right from top to bottom are corresponding phase space plots which have been calculated with space charge. These two sets of phase space plots represent the cases at $E_{DC}/E_T = 0.339$ in Fig. 10.

The top pair of phase space plots shows the position of the particles in phase space at a point along the tube just before the electron trajectories start crossing over one another. Prior to this point along the tube the velocity perturbation is approximately sinusoidal in $\phi - \theta$ and the shapes of the phase space plots are the same for both sets of calculations.

The next pair of plots shows the phase space positions when the electron trajectories start crossing over. In the calculation not including space charge shown on the left, the particles are very close to each other near $\phi - \theta = 4.8$ forming a bunch which begins to fall back towards the center of the plot. In the calculation including space charge shown on the right, the particle positions are much different. The particles near $\phi - \theta = 3.5$ feel not only the main wave field, but also the space charge repulsion due to the particles bunched near $\phi - \theta = 4.2$. As a result they strongly decelerate and form the tail shown at $\phi - \theta = 4.0$ and $q < 0$. The main wave electric field exerts a force on the electrons to the right of the tail which, in the absence of space charge, would cause those rightmost electrons to decelerate towards the center of the well. However, since we are including the space-charge force, the space-charge force due to the tail exerts an additional force on those rightmost electrons which retards their deceleration.

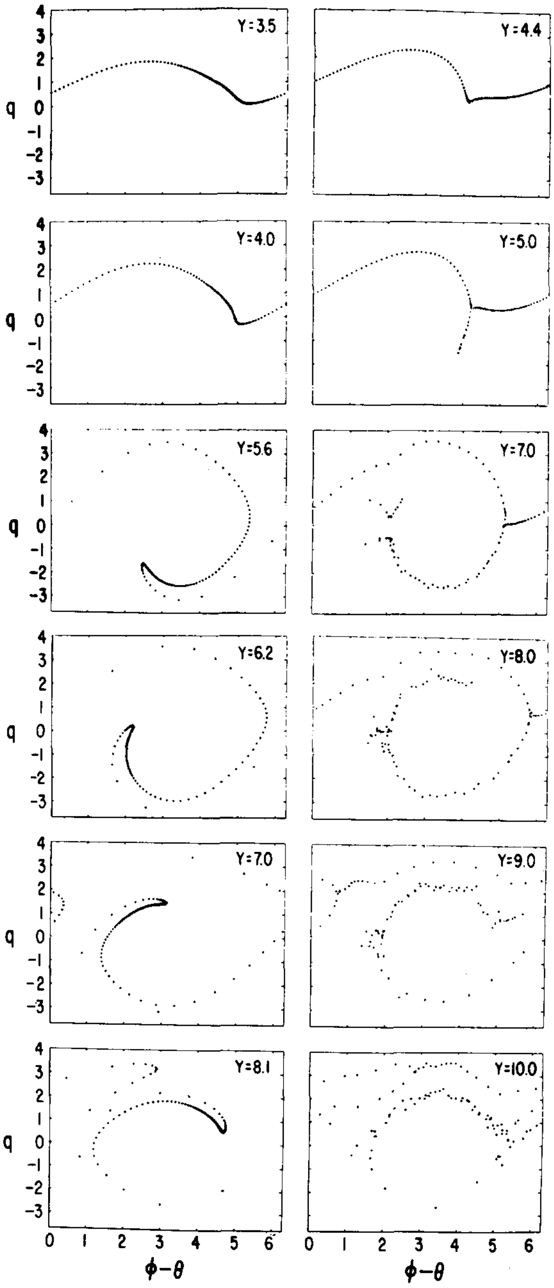

FIG. 13. Phase space plots illustrating the effect of the space-charge force. Each plot is a plot of normalized particle velocity q versus the particle phase minus the wave phase $\phi - \theta$. The left-hand column of plots represents phase space at selected positions, y, down the tube calculated in the absence of the space-charge force. The right-hand column of plots are corresponding phase space plots (although not necessarily at the same distance down the tube) calculated with the space-charge force.

The situation at saturation is shown in the third pair of plots. In the zero space-charge plot on the left, the particles continue their orbits; few, if any, get detrapped. In the finite space-charge plot on the right, many of the particles which were to the right of the tail in the middle plot have now gone over the top of the well into the next well (and appear at small $\phi - \theta$ in this plot). They have become runaway particles. The other particles remain trapped and continue to execute their rotation in phase space. The position of saturation for the zero space-charge case is $y = 5.6$ while for the finite space-charge case it is $y = 7.0$. The inclusion of space charge acts to slow down the average phase space rotation.

In the fourth pair of plots the phase space rotation continues. In both the zero and finite space-charge plots, the particles at large $\phi - \theta$ move closer and closer to the edge of the well and spill over as seen in the fifth and sixth pairs of plots. The space-charge force causes there to be more particles with larger velocity near the edge of the well. At this point most all of the runaways have been generated. In the calculation with space charge a few of the particles become detrapped subsequent to this point, and a few particles may even become retrapped.

The evolution of phase space can be described in more general terms as follows. Near the beginning of the tube, the particles have a sinusoidal distribution in phase space. A little further down the tube, the particles to the right of $\phi - \theta = \pi$ begin to move down in the direction of decreasing q. Still further down the tube, the particles begin to orbit about a position near the center of the phase space diagram, that is, near $\phi - \theta = \pi$ and $q = 0$. However, some particles never make a complete 360° orbit in phase space. These particles go over the potential hill at $\phi - \theta = 2\pi$ and are detrapped. The position in phase space about which a trapped particle orbits will in general change as a function of applied field strength and distance down the tube. However, this position is always near $\phi - \theta = \pi$ and $q = 0$ for all the phase space plots presented in this paper. In the region of the tube near where particle trajectories first begin to cross one another, there are particles which are far away from the center of the phase space orbits, and there are those which are close to the center of the phase space orbits. Most of the particles which eventually are detrapped are in a region of phase space far from the center of the phase space orbits. The effect of the beam space charge is to increase the number of electrons that are far away from the center of the phase space orbits.

E. Other configurations

We have also investigated the wave power enhancement theoretically for configurations other than that corresponding to the experiment. Figure 14 shows a plot of secular growth versus static electric field strength for various theoretical models. For reference the computed points of Fig. 10 have been represented as curve (a) in order to include the results for the experimental configuration where the static electric field is applied throughout the entire length of the slow wave structure, and where the wave is launched well below the saturation level. If we instead apply the static electric field only in the region beyond the position of saturation, the result is curve (b). In other words, we allow the wave to grow up exponentially and deeply trap the beam in the absence of the applied field. We then apply the static field for the remainder of the nonlinear region. This is the configuration that Morales originally studied in the small cold beam plasma description of the effect. It is seen that the wave power enhancement is significantly increased over that represented by curve (a). The maximum secular growth rate has been substantially increased, and the range of static field strengths over which enhancement occurs has been greatly extended.

The reason for this improvement in wave power enhancement is that the presence of the static field in the linear region causes the beam electrons to be shifted into an unfavorable region of the wave potential well while in the configuration of curve (b) the beam is allowed to be deeply trapped before feeling the applied field. At saturation the average particle velocity relative to the wave is minimized, and in this configuration most of the particles are close to the center of the phase space orbits. They are in the region near $\phi - \theta = \pi$ and $q < 0$. Any moderate increase in velocity caused by the applied static field acts to bring the particles closer to the center of the phase space orbits. In addition, the wave potential well depth is maximum at saturation. Thus, a large force can be applied from this point without causing much detrapping.

In Fig. 14, curve (c) shows the result of the highly idealized situation where a single electron is placed in a large amplitude wave. The static electric field is applied throughout the entire length of the tube, but the wave is launched at a high level. The wave enhancement is maximally efficient in

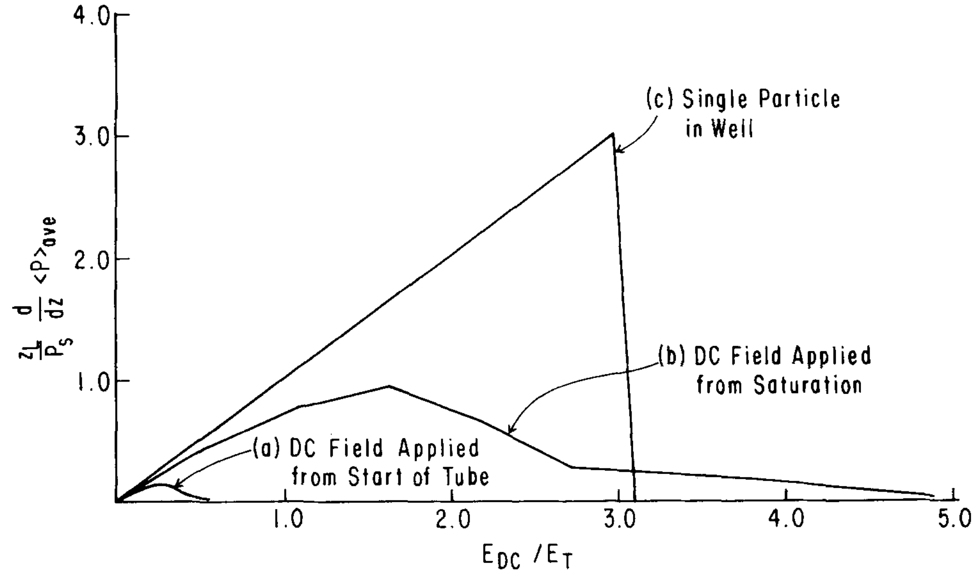

FIG. 14. Normalized secular growth rate, $(z_L/P_s)\,(d/dz)\langle P\rangle_{av}$ versus normalized static field strength E_{DC}/E_T for various theoretical models. The Pierce parameters are the same as those in Fig. 10.

this case up to $E_{DC}/E_T = 3.0$ where the enhancement abruptly falls as the particle becomes detrapped and becomes a runaway.

F. Effect of launch amplitude

If the wave is launched well below saturation, then near the beginning of the tube the wave is not large enough to trap the beam, and in this region the response of the beam to the applied static field is an acceleration. Some of the electrons then become trapped and contribute to the wave power enhancement; others become runaways.

We have found that the wave power enhancement is significantly increased when the input rf drive level is increased. The increase in the drive level results in a decrease in the length of the linear region of the tube and an increase in the wave potential throughout the region of the tube prior to saturation. This causes the electrons to be more deeply trapped and results in the production of fewer runaway electrons.

In Fig. 15 we show a plot of wave power versus axial distance for various input rf drive levels. The curve labeled SAT corresponds to a wave launched at the saturation level. SAT-2.6 indicates that the wave is launched 2.6 dB below the launch level of the SAT curve, etc. We determine the SAT level as follows. A wave is launched at a level well below the saturation level of the wave and a power plot is produced (for example, the plot labeled SAT-26). Then the beam is turned off and the transmitter power level is increased until at the position of saturation, the received power level (dotted curve at $z = 87$ cm) is equal to the saturated power level (solid curve at $z = 87$ cm). The beam is then turned back on, and the resulting plot is the curve labeled SAT. Attenuators are placed in the transmitter circuit to successively reduce the rf input drive level. In Fig. 15 we see that due to the presence of cold circuit damping, as the rf drive level increases, the saturation amplitude increases (except for the SAT-13 curve). More importantly, the position of saturation moves closer and closer to the transmitter position as the rf drive level increases, and the wave field throughout the region prior to saturation becomes larger and larger.

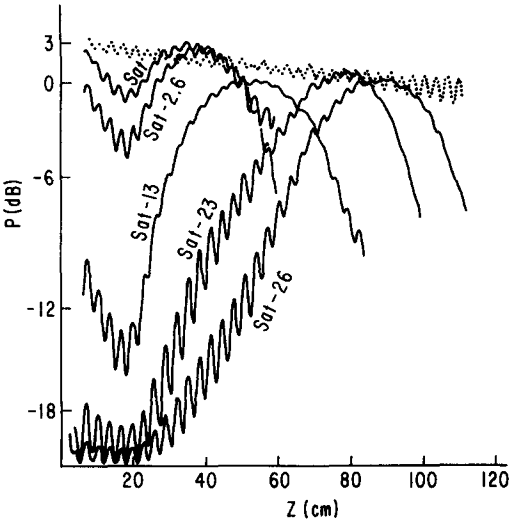

FIG. 15. Wave power versus axial distance for various input rf drive levels. The experimental and Pierce parameters are the same as those in Fig. 10. 0 dB corresponds to 0.955 mW.

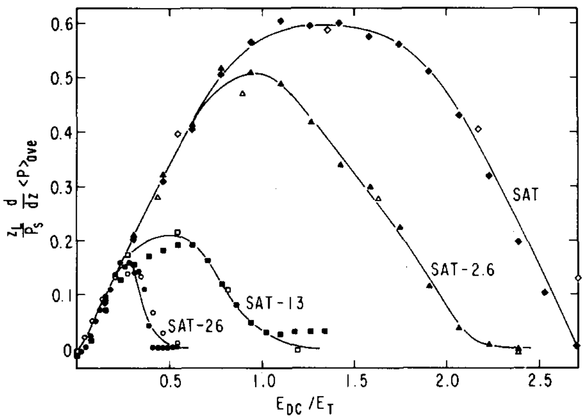

FIG. 16. Normalized secular growth rate, $(z_L/P_s)(d/dz)\langle P\rangle_{av}$ versus normalized static field strength, E_{DC}/E_T for various input rf drive levels. The Pierce parameters correspond to those in Fig. 10. The solid symbols are the results of the measurements and the open symbols are the calculated results. The lines are drawn only to aid the eye in following the trend of the data.

In Fig. 16 we plot the secular growth rate versus applied field parameterized by the rf drive level. The curve of Fig. 10 is reproduced here (labeled SAT-26). So as the drive level increases, it is seen that the wave power enhancement greatly increases in both the maximum obtainable secular growth rate and also in the range of applied electric field over which enhanced growth occurs. In the SAT-2.6 and SAT cases the secular growth rates start decreasing when applied fields of the order of E_T are applied. The solid symbols are the result of the experiment, and the open symbols are the result of the computer simulation for the corresponding Pierce parameters. The experimental uncertainties in the Pierce parameters have been discussed earlier. At low values of the wave launch level the launch amplitude is made uncertain by the presence of the reflected wave. For the SAT-26 data the uncertainty in the launch level is $\pm$ 2.0 dB. For the rest of the data the uncertainty is less than $\pm$ 0.5 dB. The input parameters of the simulation runs that produce the computed points in Fig. 16 are equal to the corresponding parameters of the experiment within experimental error. The solid lines are drawn only to aid the eye in following the trend of the points.

In Fig. 17 we compare the phase space evolution of the particles when $E_{DC}/E_T = 0.543$ for the launch level at saturation (SAT) at left and for the wave launched 26 dB below saturation (SAT-26) at right. Each pair of plots corresponds to the same axial position along the tube.

The top pair of plots shows phase space at $y = 0.2$ where the velocity perturbation in both cases is harmonic. The perturbation for the large amplitude wave launch on the left is seen to be larger than that for the small wave launch on the right.

In the next pair of plots in Fig. 17, the SAT plot on the left shows the phase space when the electron trajectories start crossing over. There are a large number of particles near the point $\phi - \theta = \pi$, $q = 0$. The SAT-26 plot on the right shows particles slightly elevated above $q = 0$ with a harmonic perturbation superimposed.

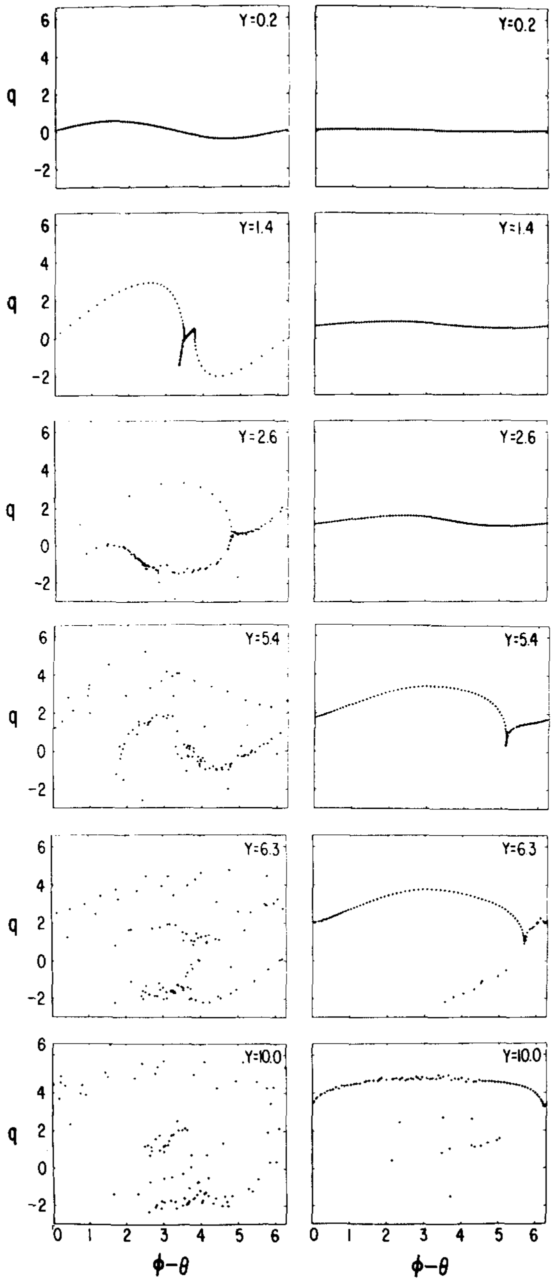

FIG. 17. Phase space plots illustrating the effect of launched wave amplitude. The left-hand column represents plots at selected positions down the tube corresponding to the open diamond (wave launched at saturation) at $E_{DC}/E_T = 0.543$ in Fig. 16. The right-hand column represents plots at the same position down the tube but corresponding to the open circle (wave launched 26 dB below saturation) at $E_{DC}/E_T = 0.543$ in Fig. 16.

The next pair of plots shows the situation at $y = 2.6$ which corresponds to the position of saturation for the SAT case on the left. It is seen in this plot that there are many particles executing tight orbits about $\phi - \theta \simeq \pi, q = 0$. In the SAT-26 plot on the right, the particles continue their rise in phase space while the wave perturbation increases.

At $y = 5.4$, the trapped particles in the SAT plot on the left continue their tight orbits. A small runaway population is also seen. In the SAT-26 plot on the right, the electron trajectories are beginning to cross over. The electrons in this case are all quite far away from the point $\phi - \theta = \pi, q = 0$.

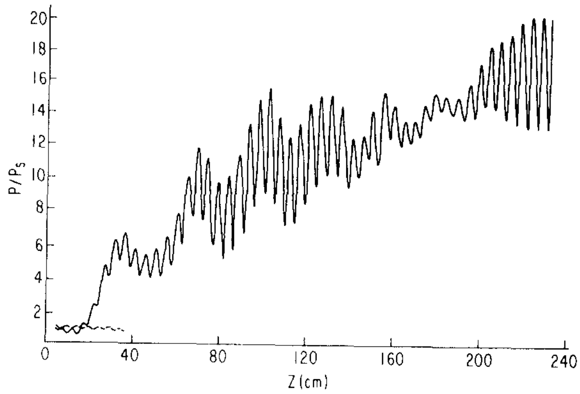

FIG. 18. Wave power (linear scale) versus axial distance for a launched large amplitude wave with a static field applied. $E_{DC} = 1.88$ V/cm, $V_0 = 55.7$ V, $I_0 = 0.5$ mA, $\omega/2\pi = 45.0$ MHz. $P_s = 5.36$ mW. The dashed curve indicates the saturation level for $E_{DC} = 0$.

The situation at $y = 6.3$ is shown in the next pair of plots. In the SAT plot on the left, the large, well-trapped electron population and the small runaway population continue to separate. The SAT-26 plot on the right shows the phase space near the position of saturation for this case. The electrons all continue to be far away from $\phi - \theta = \pi, q = 0$.

In the last pair of plots in Fig. 17, there are well-separated trapped and runaway populations in both plots. Beyond this position along the tube, the trapped and runaway electron populations continue to separate, and the rest of the essential features of the plots remain unchanged.

Slight improvement in the wave power enhancement can be produced by reducing the injected beam velocity. However, the amount by which the injected beam velocity can be reduced is limited by the sensitive dependence of the linear growth rate on velocity for a given frequency. Moreover, even if the injected beam velocity could be reduced to zero, in the small amplitude launch case the linear region would be so long that for moderate values of static field, the electrons could still be detrapped in the same manner as described above. Thus, the better way of avoiding this detrapping process is by decreasing the length of the linear region. The increase in the rf input drive level also causes an increase in the wave amplitude in this region of the tube; that is, it deepens the well. This also helps to prevent detrapping.

The maximum amount of wave power enhancement we have observed is greater than 10 dB. In Fig. 18 we exhibit our best case of wave power enhancement. The data have been placed on a linear power scale to dramatize the effect. The dashed curve on this plot indicates the level of saturation. It is seen that the wave power has overcome the dissipation due to the helix support structure and has grown to nearly 20 times the saturation power.

V. CONCLUSIONS

We have demonstrated that the wave power in a TWT can be enhanced above its saturation value by an application of a static electric field to the trapped beam electrons in the nonlinear interaction region of the TWT. When the electric field is made sufficiently strong, the beam electrons are detrapped, and the wave power enhancement is destroyed.

When the sense of the electric field is reversed, enhanced damping results.

In order to quantify the extent of the wave power enhancement, we analyze the data in a way which assigns a slope to the wave power enhancement in the nonlinear regime. Good agreement is found between theory and experiment.

The space-charge force is found to play a very important role in the detrapping mechanism. This is so because unlike the situation in a small cold beam plasma system, the space-charge force in our TWT is comparable to the force exerted by the main wave. In the calculations neglecting the beam space-charge force, the electrons near the edge of the potential well can easily decelerate toward the center of the well. In the calculations including the beam space-charge force, the motion of these electrons toward the center of the well is slowed down. These electrons are more susceptible to detrapping, and many of them slip over the edge of the well.

Our computer studies have shown that the wave power enhancement can be increased by applying the static field beginning from the position of saturation rather than applying the field along the entire length of the tube. At saturation the wave amplitude is a maximum and the average beam velocity is a minimum. Under these conditions it is very difficult to detrap the beam particles.

The wave power enhancement can also be improved by increasing the input rf drive level which decreases the length of the linear region and increases the wave potential throughout the region of the tube prior to saturation. An examination of phase space shows that this acts to prevent the electrons from entering unfavorable regions of phase space. We have found that by launching near the saturation level, the wave power can be enhanced by more than 10 dB.

ACKNOWLEDGMENTS

We are grateful to Professor Norman Kroll and Professor Thomas O'Neil for several valuable conversations. We also appreciate discussions with Professor George Morales; his work provided the initial impetus for this research. In addition, the technical assistance of Gary Smith and Ralph Dawson is greatly appreciated.

This paper is based on a dissertation submitted by Stanley I. Tsunoda to the University of California at San Diego in partial fulfillment of the requirements for the Ph.D. degree.

This material is based upon work supported by the National Science Foundation under Grants PHY77-20613 and PHY80-09326.

APPENDIX: RELATIONSHIP BETWEEN THE SMALL COLD BEAM PLASMA EQUATIONS AND THE TWT EQUATIONS

The spatial small cold beam plasma equations were first derived and solved by O'Neil and Winfrey.[9] The TWT large signal equations used in this paper are extensions (by Hess) of the work by Tien. The following shows the relationship between the small cold beam plasma equations and the TWT equations. Detuning, damping, space charge, and finite beam strength corrections are included.

The appendix is divided into five parts. The first part extends the analysis of O'Neil and Winfrey to include detuning, damping, and space charge. The second part shows the relationship between the small cold beam plasma parameter $\eta'/2$ and Pierce's gain parameter C. The third part derives a set of TWT equations[25] from the small cold beam plasma equations. The fourth part presents an additional refinement to the TWT theory due to Tien[16]—the finite beam strength correction term. The fifth part discusses the treatment and relative strength of the space-charge force in the two theories.

1. Spatial small cold beam-plasma equations

The physics of the interaction between a small cold electron beam and a plasma is simplified in an important way by the introduction of the single wave model[8]. If the temperature of the electron beam is sufficiently low and if the density is sufficiently small, then after a few e-foldings, the bandwidth of the growing waves is so narrow that the spectrum is very nearly a single wave. Under these conditions it has been shown[8] that the background plasma electrons continue to execute linear oscillations even when the wave amplitude is so large that the dynamics of the beam electrons are highly nonlinear. Thus, the plasma may be treated as a linear dielectric, and the plasma charge density may be represented by a dielectric function.

Consider a potential $\Phi_{\text{total}}(z,t)$ of the form

$$\Phi_{\text{total}} = \tfrac{1}{2}[\Phi(z,t) + \Phi_{SC}(z,t) + \Phi_{DC}(z) + \text{c.c.}] . \quad \text{(A1)}$$

The first term is associated with the spatially growing main wave

$$\Phi(z,t) = \Phi(z)\exp[i\omega(z/u_0 - t)] ,$$
$$\Phi(z) = \Phi(0)\exp\left(i\int_0^z dz'\,\delta k(z')\right), \quad \delta k(z) \ll \omega/u_0 . \quad \text{(A2)}$$

Here $\delta k(z)$ is a spatially varying complex wavenumber correction to ω/u_0. The second term represents the harmonic field contribution

$$\Phi_{SC}(z,t) = \sum_{n=1}^{\infty} \Phi_{SC}(z,\omega_n)e^{-i(n+1)\omega t} . \quad \text{(A3)}$$

The third term corresponds to the applied static electric field

$$\Phi_{DC}(z) = -E_{DC}z . \quad \text{(A4)}$$

The beam is divided into N charge sheets per period. The beam density is given by

$$n_b(z,t) = \frac{2\pi u_0}{\omega}\frac{\bar{n}_b}{N}\sum_{j=1}^{N}\delta[z - z_j(t)] , \quad \text{(A5)}$$

where $\bar{n}_b$ is the unperturbed beam density (per unit volume) and $z_j(t)$ is the position of the jth charge sheet. To be consistent with the expression for the potential

$$n_b(z,t) = \tfrac{1}{2}[n_b(z,\omega)e^{-i\omega t} + \text{c.c.}] , \quad \text{(A6)}$$

with

$$n_b(z,\omega) = \frac{2u_0\bar{n}_b}{N}\sum_{j=1}^{N}\frac{e^{i\omega t_j}}{(dz/dt)_j} , \quad \text{(A7)}$$

t_j is the time at which the jth electron is at the position z. We assume the dielectric function is not resonant at ω/u_0 but at a different wavenumber $k_0 = (1 + \Delta_1)\omega/u_0$, where $|\Delta_1| \ll 1$. The wave in the beam plasma system has wavenumber $\omega/u_0 + \delta k$. So the plasma dielectric function, $\epsilon(\omega,k)$, near resonance is

$$\epsilon\left(\omega, \frac{\omega}{u_0} + \delta k\right) \cong \left(\frac{\partial\epsilon}{\partial k}\right)_{\omega,k_0}\left(\delta k - \frac{\omega}{u_0}\Delta_1\right). \tag{A8}$$

Poisson's equation then becomes

$$\begin{aligned}&\frac{\omega^2}{u_0^2}\left(\frac{\partial\epsilon}{\partial k}\right)_{\omega,k_0}\left(\delta k - \frac{\omega}{u_0}\Delta_1\right)\Phi(z)\\ &\quad = \frac{-8\pi e u_0 \bar{n}_b}{N}\sum_{j=1}^{N}\frac{e^{-i\omega(z/u_0 - t_j)}}{(dz/dt)_j}.\end{aligned} \tag{A9}$$

This equation corresponds to Eq. (16) of O'Neil and Winfrey.[9] Let us define

$$\begin{aligned}\Phi(z) &= \phi_1(z)\exp\left(i\int_0^z dz'\,\delta k_r(z')\right),\\ \phi_1(z) &= \phi_1(0)\exp\left(-\int_0^z dz'\,\delta k_i(z')\right),\end{aligned} \tag{A10}$$

where $\delta k_r = \operatorname{Re}\delta k$ and $\delta k_i = \operatorname{Im}\delta k$. Taking the real and imaginary parts of Eq. (A9) and rearranging, we obtain

$$\begin{aligned}\delta k_r - \frac{\omega}{u_0}\Delta_{1r} &= \frac{-8\pi e u_0 \bar{n}_b}{N(\omega^2/u_0^2)(\partial\epsilon/\partial k)_{\omega,k_0}}\frac{1}{\phi_1}\\ &\quad\times\sum_{j=1}^{N}\frac{\cos[(\omega/u_0)z - \omega t_j + \int_0^z dz'\,\delta k_r]}{(dz/dt)_j},\end{aligned} \tag{A11a}$$

$$\begin{aligned}\frac{d\phi_1}{dz} &= \frac{-8\pi e \bar{n}_b u_0}{N(\omega^2/u_0^2)(\partial\epsilon/\partial k)_{\omega,k_0}}\\ &\quad\times\sum_{j=1}^{N}\frac{\sin[(\omega/u_0)z - \omega t_j + \int_0^z dz'\,\delta k_r]}{(dz/dt)_j} - \frac{\omega}{u_0}\Delta_{1i}\phi_1,\end{aligned} \tag{A11b}$$

where $\Delta_{1r} = \operatorname{Re}\Delta_1$ and $\Delta_{1i} = \operatorname{Im}\Delta_1$. We also have Newton's equation

$$m\left(\frac{d^2z}{dt^2}\right)_j = e\frac{\partial}{\partial z}\Phi_{\text{total}}(z,t_j). \tag{A12}$$

Equations (A11) and (A12) are the small cold beam plasma equations in the spatially growing case.

2. Relation between C and $\eta'/2$

Here we show that if we identify the slow wave structure impedance with the plasma impedance, then C is equivalent to $\eta'/2$, the spatial small cold beam plasma parameter.

The slow wave structure interaction impedance is defined as $R = \langle E_z^2\rangle_b/2k_{0r}^2 P$, where $k_{0r} = \operatorname{Re} k_0$ and $\langle E_z^2\rangle_b$ is the z component of the electric field averaged over the beam cross-sectional area A_b.

$$\langle E_z^2\rangle = \frac{1}{A_b}\int E_z^2\,dA_b, \tag{A13}$$

P is the power given by

$$P = \frac{c}{8\pi}\operatorname{Re}\int (E \times H^*)d\tau, \tag{A14}$$

where the integral is over the plane perpendicular to the direction of propagation.

In the one-dimensional plasma it is useful to define

$$P = \int v_g \mathscr{E}\,d\sigma, \tag{A15}$$

where

$$\mathscr{E} = \frac{1}{16\pi}\omega\left(\frac{\partial\epsilon}{\partial\omega}\right)_{\omega,k_0}|E_z^2| \tag{A16}$$

is the wave energy density, v_g is the group velocity, and we integrate over the plane perpendicular to the direction of propagation. The plasma impedance then is

$$R_{\text{plasma}} = \frac{-8\pi}{k_{0r}^2\omega(\partial\epsilon/\partial k)_{\omega,k_0}A_P}. \tag{A17}$$

The beam impedance is

$$\frac{V_0}{I_0} = \frac{2\pi u_0}{A_b\omega_p^2}\frac{n_0}{\bar{n}_b}, \tag{A18}$$

where n_0 is the plasma density and $\bar{n}_b$ the beam density. So letting $R = R_{\text{plasma}}$,

$$\begin{aligned}C^3 &= \frac{I_0 R_{\text{plasma}}}{4V_0}\\ &= -\frac{\omega_p^2}{\omega^2}\frac{\bar{n}_b}{n_0}\frac{1}{(u_0/\omega)k_{0r}^2(\partial\epsilon/\partial k)_{\omega,k_0}}.\end{aligned} \tag{A19}$$

In O'Neil and Winfrey $k_{0r} = \omega/u_0$. So

$$C^3 = (\eta'/2)^3. \tag{A20}$$

3. Equations of the TWT

Using the identification

$$\begin{aligned}C^3 &= \frac{I_0 R}{4V_0} = \left(\frac{\eta'}{2}\right)^3\\ &= \frac{-\omega_p^2}{\omega^2}\frac{\bar{n}_b}{n_0}\frac{1}{(\partial\epsilon/\partial k)_{\omega,k_0}k_{0r}^2(u_0/\omega)},\end{aligned} \tag{A21}$$

we can now define the scaled TWT variables. The initial phase is

$$\phi_0 = \omega T_{0j}, \tag{A22}$$

where T_{0j} is the time at which the jth electron enters the tube at $z = 0$. As such ϕ_0 can be regarded as identifying a particular electron. The phase is given by

$$\phi(y,\phi_0) = \omega(z/u_0 - t_j). \tag{A23}$$

The velocity is given by

$$\left(\frac{dz}{dt}\right)_j = u_0[1 + Cq(y,\phi_0)]. \tag{A24}$$

The scaled wave potential $A(y)$ is given by

$$\phi_1(z) = 4C^2 V_0 A(y), \tag{A25}$$

and the wave phase is

$$\theta(y) = -\int_0^z dz'\,\delta k_r(z'). \tag{A26}$$

The Pierce detuning parameter b and damping parameter d are related to the complex quantity Δ_1. Since

$$k_0=(1+\Delta_1)\omega/u_0,$$

$$\begin{aligned}&\operatorname{Re} k_0=k_{0r}=(\omega/u_0)(1+\Delta_{1r}),\\ &\Delta_{1r}=(u_0-v_0)/v_0=Cb,\end{aligned} \qquad \text{(A27)}$$

where v_0 is the phase velocity ω/k_{0r}, and

$$\begin{aligned}&\operatorname{Im} k_0=k_{0i}=(\omega/u_0)\Delta_{1i},\\ &\Delta_{1i}=Cd.\end{aligned} \qquad \text{(A28)}$$

Substitution of Eqs. (18), (A22)–(A28) into Eq. (A11) and converting sums to integrals yields two of the TWT equations—Eqs. (25) and (26). Substituting Eqs. (18), (A22)–(A28) into Eq. (A12) gives

$$\begin{aligned}(1+Cq_j)\frac{\partial q_j}{\partial y}&=2A\sin(\phi-\theta)\\ &\quad-2C\left(A\frac{d\theta}{dy}\sin(\phi-\theta)+\frac{dA}{dy}\cos(\phi-\theta)\right)\\ &\quad-\frac{e}{m\omega u_0C^2}(E_{\rm SC}+E_{DC}),\end{aligned} \qquad \text{(A29)}$$

where we have identified the harmonic fields with the space-charge field. Finally, we note that since $\phi=\omega(z/u_0-t_j)$

$$\left(\frac{dz}{dt}\right)_j=\frac{u_0}{1-C(\partial\phi/\partial y)}, \qquad \text{(A30)}$$

equating this expression with Eq. (A24) yields Eq. (27). Equations (25), (26), (27), and (A29) are a set of equations for the TWT. They correspond to Eqs. (14), (21), (22), and (23) of Rowe.[25] Equations (25) and (26) are lower-order versions of Rowe's (21) and (22).

In order to obtain the set of equations used in this paper, the finite beam strength correction must be included.

4. Finite beam strength correction

In TWT theory the starting point for the theory is not Poisson's equation but an inhomogeneous wave equation,

$$\begin{aligned}&\frac{\partial^2V_{\rm circ}}{\partial z^2}-\frac{k_{0r}^2}{\omega^2}\frac{\partial^2V_{\rm circ}}{\partial t^2}-\frac{2k_{0r}k_{0i}}{\omega}\frac{\partial V_{\rm circ}}{\partial t}\\ &\quad=\frac{-Zk_{0r}}{\omega}\left(\frac{\partial^2\rho}{\partial t^2}+\frac{k_{0i}\omega}{k_{0r}}\frac{\partial\rho}{\partial t}\right),\end{aligned} \qquad \text{(A31)}$$

where $\rho(z,t)$ is the beam charge density and

$$\rho(z,t)=\rho_\omega(z)e^{-i\omega t}. \qquad \text{(A32)}$$

The solution to Eq. (A31) is

$$\begin{aligned}V_{\rm circ}(z,t)&=c_1e^{i(k_0z-\omega t)}+c_2e^{-i(k_0z+\omega t)}\\ &\quad-\frac{i\omega R}{2}e^{i(k_0z-\omega t)}\int_0^z e^{-ik_0z'}\rho_\omega(z')dz'\\ &\quad-\frac{i\omega R}{2}e^{-i(k_0z+\omega t)}\int_z^D e^{ik_0z'}\rho_\omega(z')dz',\end{aligned} \qquad \text{(A33)}$$

where we have neglected the imaginary part of Z, and c_1 and c_2 are constants and the system extends from $z=0$ to $z=D$. We assume $|k_0D|\gg 1$. We assume that the beam travels in the direction of increasing z. The second term in Eq. (A33) represents a pure helix mode traveling in the opposite direction. We neglect this backward wave since it is far from synchronism with the beam. Let

$$\begin{aligned}V(z,t)&=-\frac{i\omega R}{2}e^{i(k_0z-\omega t)}\int_0^z\rho_\omega(z')e^{-ik_0z'}dz'\\ &\quad+V(0)e^{i(k_0z-\omega t)},\end{aligned} \qquad \text{(A34)}$$

$$V_c(z,t)=-\frac{i\omega R}{2}e^{-i(k_0z+\omega t)}\int_z^D\rho_\omega(z')e^{ik_0z'}dz'. \qquad \text{(A35)}$$

At first glance it might seem that we should neglect $V_c(z,t)$ altogether. However, there is a portion of $V_c(z,t)$ that is in synchronism with the beam. In the linear theory, for instance $\rho_\omega(z)=\rho_\omega(0)e^{ik_Lz}$. In this case,

$$\begin{aligned}V_c(z,t)&=-\frac{i\omega R}{2}\frac{\rho_\omega(0)}{k_L+k_0}\\ &\quad\times\{\exp[i(k_L+k_0)D]\exp[-i(k_0z+\omega t)]\\ &\quad-\exp[i(k_Lz-\omega t)]\}.\end{aligned} \qquad \text{(A36)}$$

The first term corresponds to a backward traveling lightly damped (due to cold circuit damping, k_{0i}) wave. The second term is a small forward traveling growing wave. It is much smaller than the main growing wave and is a small correction to it.

By directly substituting Eqs. (A34) and (A35) one can verify that

$$\frac{\partial V}{\partial z}+\frac{k_0}{\omega}\frac{\partial V}{\partial t}=-\frac{\partial V_c}{\partial z}+\frac{k_0}{\omega}\frac{\partial V_c}{\partial t}. \qquad \text{(A37)}$$

Let us write

$$V(z,t)=V(z)e^{i\omega(z/u_0-t)}, \qquad \text{(A38)}$$

$$V_c(z,t)=V_c(z)e^{i\omega(z/u_0-t)}. \qquad \text{(A39)}$$

Then Eq. (A37) becomes

$$-i\left(\frac{\omega}{u_0}+k_0\right)V_c=i\left(\frac{\omega}{u_0}-k_0\right)V(z)+\frac{\partial V}{\partial z}+\frac{\partial V_c}{\partial z}. \qquad \text{(A40)}$$

Let us neglect $\partial V_c/\partial z$ and show later that it is small,

$$V_c(z)\cong\frac{1}{\omega/u_0+k_0}\left[i\frac{\partial V(z)}{\partial z}-\left(\frac{\omega}{u_0}-k_0\right)V(z)\right]. \qquad \text{(A41)}$$

Since $k_0=k_{0r}+iC\,d\omega/u_0$,

$$V_c(z)\cong\frac{v_0}{2\omega}\left[i\left(\frac{\omega}{u_0}C\,dV(z)+\frac{\partial V}{\partial z}\right)-\frac{\omega}{u_0}Cb\,V(z)\right]. \qquad \text{(A42)}$$

Let

$$\begin{aligned}&V(z)=\phi_1(z)\exp\left(i\int_0^z dz'\,\delta k_r(z')\right),\\ &\phi_1(z)=\phi(0)\exp\left(-\int_0^z dz'\,\delta k_i(z')\right)=4C^2A(y)V_0,\end{aligned} \qquad \text{(A43)}$$

substituting (A43) into (A42), making use of (A26) and (A27), and taking the real part yields Eq. (24). We have neglected terms of order (C^3d). The correction due to finite beam strength is one order of C smaller than the main wave, and $\partial V_c/\partial z$ is correspondingly smaller.

When the main wave expression and the finite beam strength correction are inserted into Eq. (A31), each term on the left-hand side consists of a main wave contribution and a correction term of order C smaller. When the two correction terms are subtracted the result becomes an order of C^2 smaller than the main wave contribution. Thus, the two equations which are derived from the wave equation [Eqs. (25) and (26)] are not affected to order C by the addition of $V_c(z,t)$. When Eq. (24) is included in the expression for Φ_{total} and substituted into Eq. (A12), the result is the TWT equation, Eq. (28).

5. The space-charge force in the beam plasma and TWT

We have found so far that the equations of the spatial small cold beam plasma interaction become nonlinear TWT equations when the Pierce gain parameter C is identified with the spatial small cold beam plasma parameter $\eta'/2$. In our experiment C is typically around 0.1. This is also a typical value for $\eta'/2$ in small cold beam plasma experiments. However, the way in which C is made small is different in our experiment than the way in which $\eta'/2$ is made small in a typical plasma experiment. Let us rewrite C in a way which allows a more direct comparison with $\eta'/2$.

$$C^3 = \frac{\omega_b^2}{\omega^2} \frac{A_b R \omega^2}{8\pi u_0}, \tag{A44}$$

$$\left(\frac{\eta'}{2}\right)^3 = -\frac{\omega_b^2}{\omega^2} \left(\frac{u_0}{\omega} k_{0r}^2 \frac{\partial \epsilon}{\partial k}\right)^{-1}, \tag{A45}$$

where $\omega_b^2 = \omega_p^2(\bar{n}_b/n_0)$ and A_b is the beam cross-sectional area. For a cold infinite plasma

$$-\frac{u_0}{\omega} k_{0r}^2 \frac{\partial \epsilon}{\partial k} = \frac{4}{3}. \tag{A46}$$

In our experiment, typically,

$$A_b R \omega^2 / 8\pi u_0 = \tfrac{1}{79}. \tag{A47}$$

Thus the beam charge density in our TWT must be correspondingly larger in order for C and $\eta'/2$ to be equal. One manifestation of this difference is the size of the space-charge force in the two systems. In the small cold beam plasma system, the harmonic fields are always a factor of $\eta'/2$ smaller than in the main field of the wave. However, as seen in Fig. 12, in a TWT the space-charge field can be comparable to the main wave electric field.

One way to estimate the size of the maximum space-charge force is to consider a delta function distribution of charge and consider the size of the resulting electric field compared to the size of the main wave field. For the beam-plasma case

$$E_{\text{SC}} \sim 2\pi e \bar{n}_b \lambda = \frac{4\pi^2 e \bar{n}_b u_0}{\omega} = \pi \frac{4\pi n_0 e^2}{m} \frac{m u_0}{\omega e} \frac{\bar{n}_b}{n_0}, \tag{A48}$$

where $\bar{n}_b$ and n_0 are the beam and plasma densities.

$$= 2\pi \frac{\omega_p^2}{\omega^2} \left(-\frac{\omega}{u_0} V_0\right) \left(\frac{\bar{n}_b}{n_0}\right). \tag{A49}$$

Since

$$\left(\frac{\eta'}{2}\right)^3 \cong \frac{\omega_p^2}{\omega^2} \frac{\bar{n}_b}{n_0} = -2\pi \left(\frac{\eta'}{2}\right)^3 \frac{\omega}{u_0} V_0, \tag{A50}$$

and

$$\begin{aligned} E_T &= 2\left(\frac{\eta'}{2}\right)^2 \frac{\omega}{u_0} V_0, \\ \frac{E_{\text{SC}}}{E_T} &= -\pi \frac{\eta'}{2}. \end{aligned} \tag{A51}$$

As expected, the space-charge electric field is of order $\eta'/2$ smaller than the main wave field even for a delta function charge distribution. However, for the TWT

$$E_{\text{SC}} \sim 2\pi e \bar{n}_b \lambda = \frac{4\pi^2 e \bar{n}_b u_0}{\omega} = \frac{4\pi^2}{2C^2} \frac{\bar{n}_b e u_0^2}{\omega^2 V_0} E_T. \tag{A52}$$

Since $E_T = 2(\omega/u_0)C^2 V_0$,

$$\frac{E_{\text{SC}}}{E_T} = -\pi \frac{1}{C^2} \frac{\omega_b^2}{\omega^2}. \tag{A53}$$

Typically, $\omega_b/\omega \sim 1/4$ and $C \sim 0.1$, so

$$|E_{\text{SC}}/E_T| \sim 20. \tag{A54}$$

Given a delta function charge distribution, one can also estimate the ratio of the harmonic fields to the field of the main wave. One obtains essentially the same scalings as before.

Another way of expressing the difference between the small cold beam plasma system and a typical TWT is to consider the Pierce gain parameter and the small cold beam plasma smallness parameter as the ratio of impedances. The Pierce gain parameter is the cube root of the ratio of the slow wave structure interaction impedance to the beam impedance. The smallness parameter is the cube root of the ratio of the plasma impedance to the beam impedance. The helix impedance is much smaller than the plasma impedance and this causes the beam impedance in the TWT to be much smaller than the beam impedance in the beam plasma system in order to have C and $\eta'/2$ be equal. This in turn results in a larger beam space-charge field in the TWT.

[1] R. L. Hess, Ph.D. thesis, University of California, 1960 (unpublished).

[2] G. J. Morales, Phys. Fluids **23**, 2472 (1980).

[3] N. M. Kroll, P. Morton, and M. N. Rosenbluth, in *Physics of Quantum Electronics*, edited by S. Jacobs, M. Sargent, and M. Scully (Addison-Wesley, Reading, MA, 1980), Vol. 7, Chaps. 4, 5, and 6.

[4] A. T. Lin, Phys. Rev. Lett. **46**, 1515 (1981).

[5] J. R. Pierce, *Traveling Wave Tubes* (Van Nostrand, New York, 1950).

[6] O. Sauseng, Nachrichtentech. Fachber. **35**, 16 (1968).

[7] J. G. Meeker and J. E. Rowe, IRE Trans. Electron Devices **9**, 257 (1962).

[8] T. M. O'Neil, J. H. Winfrey, and J. H. Malmberg, Phys. Fluids **14**, 1204 (1971).

[9] T. M. O'Neil and J. H. Winfrey, Phys. Fluids **15**, 1514 (1972).

[10] L. R. Elias, W. M. Fairbank, J. M. J. Madey, H. A. Schwettman, and T. I. Smith, Phys. Rev. Lett. **36**, 717 (1976).

[11] N. Kroll, in Ref. 3, Vol. 5, Chap. 3.

[12] C. Menyuk, D. Hammer, and G. J. Morales, Bull. Am. Phys. Soc. **22**, 1200 (1977).

[13] D. Hammer, N. C. Luhmann, and G. J. Morales, Bull. Am. Phys. Soc. **22**, 1201 (1977).

[14] J. N. Leboeuf and T. Tajima, Phys. Fluids **22**, 1485 (1979).
[15] A. Nordsieck, Proc. IRE **41**, 630 (1953).
[16] P. K. Tien, Bell Syst. Tech. J. **35**, 349 (1956).
[17] P. K. Tien, L. R. Walker, and V. M. Wolontis, Proc. IRE **43**, 260 (1955).
[18] C. K. Birdsall and G. R. Brewer, IRE Trans. Electron Devices **ED-1**, 1 (1954).
[19] G. M. Branch and T. G. Mihran, IRE Trans. Electron Devices **ED-2**, 3 (1955).
[20] G. Dimonte and J. H. Malmberg, Phys. Fluids **21**, 1188 (1978).
[21] J. H. Malmberg, T. H. Jensen, and T. M. O'Neil, in *Plasma Physics and Controlled Nuclear Fusion Research* (IAEA, Vienna, 1966), Vol. I, p. 683.
[22] See, for example, J. H. Malmberg and C. B. Wharton, Phys. Rev. Lett. **17**, 175 (1966).
[23] R. Kompfner, J. Brit. IRE **10**, 283 (1950).
[24] H. R. Johnson, Proc. IRE **43**, 874 (1955).
[25] J. E. Rowe, IRE Trans. Electron Devices **3**, 39 (1956).